New Tools for Terrain Gravimetry
NEWTON-g
Project number: 801221

Deliverable 4.5

Data usage for hazard analysis

Lead beneficiary:	University of Geneva
Dissemination level:	Public
Version	Final

NEWTON-g has received funding from the EC's Horizon 2020 programme, under the FETOPEN-2016/2017 call (Grant Agreement No. 801221)

Document Information

Grant Agreement Number	801221
Acronym	NEWTON-g
Start date of the project	1 June 2018
Project duration (months)	48 (extended to 54)
Deliverable number	D4.5
Deliverable Title	Data usage for hazard analysis
Due date of deliverable	30 September 2022
Actual submission date	24/10/2022
Lead Beneficiary	University of Geneva
Type	R: Document, report
Dissemination level	PU - Public
Work Package	WP4 – Data analysis

Version	Date	Author	Comments
v.0	02/09/2022	V. Freret-Lorgeril, C. Bonadonna, C. Frischknecht	Creation
v.1	23/09/2022	L. Passarelli, E. Rivalta, M. Nikkhoo,	1st revis.
v.2	04/10/2022	V. Freret-Lorgeril, D. Carbone	2nd revis.
v.3	07/10/2022	L. Passarelli, V. Freret-Lorgeril, D. Carbone, E. Rivalta. C. Bonadonna	3rd revis.
Final	21/10/2022	L. Passarelli, V. Freret-Lorgeril, E. Rivalta, M. Nikkhoo, C. Frischknecht, C. Bonadonna, D. Carbone	Validation

Contents

1 Overview and motivation

One of the targets of NEWTON-g is exploring the potential of gravity data from volcanoes for hazard analysis purposes. Indeed, given the unique insights into subsurface fluids it provides, gravimetry may supply useful information for characterizing the hazard potential at active volcanoes. The present document reports on the activities that have been carried out in the framework of Task 4.4 (Use of the data for hazard analysis). D4.5 was originally intended to build on the data produced by the gravity imager, after its deployment on Mt. Etna. Nevertheless, mainly due to COVID-related issues, it was not possible to install the array of MEMS gravimeters in time to produce time series that could be used in the framework of D4.5. Conversely, in the frame of NEWTON-g, the absolute quantum gravimeters (AQG-B) produced by iXblue was deployed in the summit zone of Etna in the summer of 2020 (D3.4 and Antoni-Micollier et al., 2022) and data it produced are considered in the present document (see sections 2.5.2 and 2.5.3).

Here, the possible application of gravity data to characterize volcanic hazard, is studied with a focus on lava fountains (LFs), which have been one of the most distinctive characters of Mt. Etna's volcanic activity during the last two decades. In particular, we apply two different approaches, one data-driven, the other model-driven. In the framework of the data-driven approach, we exploit the gravity data collected in 2021 through the AQG-B and the two iGrav superconducting gravimeters in the monitoring network managed by INGV-OE (Carbone et al., 2019), with the aim of (i) identifying anomalies related to the LFs which took place during most of 2021 and (ii) compare the characteristics of these anomalies to the eruption parameters retrieved by remote sensing techniques. Eruption parameters (e.g. erupted mass) are key to the assessment of volcanic hazards and the forecasting of volcanic ash. In the framework of the model-driven approach, we use a gravity time-series encompassing 9 episodes of lava fountaining during the summer of 2011 (Carbone et al., 2015), to build up plausible models for the gravity decreases preceding the LF events. For this purpose, tools developed under NEWTON-g (Nikkhoo and Rivalta, 2022a,b) are used in the time-dependent modeling of mass transport during the pre-fountaining phases. This approach is applied to build scenario-based synthetic time series of gravity changes, which are benchmarked against the gravity changes observed in 2011. The developed scenario-based models are flexible and can be used to also investigate the possible gravity effect driven by eruptive processes other than those behind LFs.

The two aforementioned approaches are also discussed in the light of the possible use of continuous gravity data in real- or near-real time applications for hazard analysis and early warning at volcanoes. We conclude that, even though a purely data-driven analysis of gravity time series holds promising potential, approaches that involve some modeling are desirable, especially to decompose the gravity time series in their fundamental parts and to associate each part to the physical processes driving mass changes.

2 Analysis of gravity data and eruptive source parameters during 2021 LFs

Valentin Freret-Lorgeril, Costanza Bonadonna, Daniele Carbone, Eleonora Rivalta, Luigi Passarelli, Stefano Corradini, Lorenzo Guerrieri, Luigi Mereu, Corine Frischknecht

Recent volcano monitoring strategies have integrated multi-sensor techniques to better evaluate the eruptive source parameters (ESPs) of explosive eruption in real time. These parameters, used to initialize ash dispersal models, include the Mass Eruption Rate (MER), the plume height, the vent location and the Total Grain-Size Distribution (TGSD) (e.g. Bonadonna et al., 2012; Scollo et al., 2019, and reference therein). Whilst remote sensing strategies allow to retrieve syn-eruptive quantitative information, they do not provide any insight on the bulk pre-eruptive processes and cannot thus inform early-warning systems. Using infrasound data from arrays close the eruptive vents at Mt. Etna, it has been possible to detect increasing explosive activity, potentially leading to paroxysmal events, based on the determination of infrasound thresholds (Ripepe et al., 2018). Nonetheless, while the ESPs are measured during and after ongoing explosive activity, no technique exists that is able to quantify the amount of mass potentially released during a paroxysm before it actually starts. Carbone et al. (2015) showed that gravimeters might capture meaningful changes $\tilde{9}$0-160 min before paroxysmal activity. Such an observation has highlighted the potential use of gravimetry for volcano early warning; indeed, it could provide, before the outbreak of the eruption, first order information on the ESPs, needed for dispersal modelling and assessments of the risk linked to tephra plume dispersion. To precisely track fast gravity changes induced by bulk volcanic processes a mini-array of continuously running iGrav superconducting gravimeters (SGs) was installed at Etna between 2014 and 2016 (Carbone et al., 2019). The AQG-B03 absolute quantum gravimeter was also installed at Etna in 2020, in the framework of NEWTON-g (Antoni-Micollier et al., 2022). Here, we focus on the possible use of data from the SGs and the AQG on Etna, with the aim to (i) test their capacity to capture physical changes prior to explosive events and (ii) evaluate the potential use of gravimeters to provide insightful information before paroxysmal episodes, based on the comparison of gravity signals with syn-eruptive remote sensing estimates.

2.1 Mt. Etna's paroxysms and the eruptive source parameters

Since 2011, the South East Crater (SEC) of Etna volcano has produced hundreds of paroxysmal episodes impacting local population and regularly disrupting air traffic to and from Catania airport (30 km away from Etna's active craters). After a 3-years long period of paroxysmal activity from SEC, during 2011 to 2013 at SEC (Behncke et al., 2014; De Beni et al., 2015), the activity at the summit craters of Etna was mostly characterized by successive phases of lava flow emission and strombolian activity, interspersed by punctual paroxysmal phases, (e.g., eruptions from la Voragine Crater in December 2015; Vulpiani et al., 2016; Calvari et al., 2018; Freret-Lorgeril et al., 2018). Starting from December 2020, a new paroxys-

mal sequence occurred at SEC, until 2022, producing more than 60 lava fountain events. Mt. Etna's paroxysmal events are often characterized by 100-1000 km high lava fountains accompanied by the emission of 9-15 km high tephra plumes and lava flows. These paroxysms generally present a similar succession of eruptive phases (Alparone et al., 2003; Behncke et al., 2014; Andronico et al., 2018; Calvari et al., 2018; Freret-Lorgeril et al., 2018). Increasing strombolian activity occurs during the first phase, followed by sustained lava fountain emission (climactic phase) and, finally, a rapid decrease of the eruptive activity (i.e., waning phase). Each paroxysmal event can be monitored through the combined use of complementary remote sensing techniques available at Mt. Etna and tephra-fallout deposit analyses, which allows the ESP determination (Andronico et al., 2014; Corradini et al., 2016; Calvari et al., 2018; Freret-Lorgeril et al., 2018, 2021; Scollo et al., 2019; Marzano et al., 2020). Underground volcanic processes occurring prior to and during lava fountains have been studied through different geophysical techniques, including ground deformation, ground-based infrared and gravity studies (e.g. Bonaccorso et al., 2014; Bonaccorso and Calvari, 2017; Carbone et al., 2015). However, it is important to note that changes observable at the surface are induced by the whole mass potentially involved in paroxysmal episodes. This includes the mass of tephra detected by remote sensing sensors but also the released gas and the emitted lava flows. Satellite infrared and visible imagery are used to retrieved the mass of SO2 and the volume of lava flow emitted during each paroxysm, respectively (see details below).

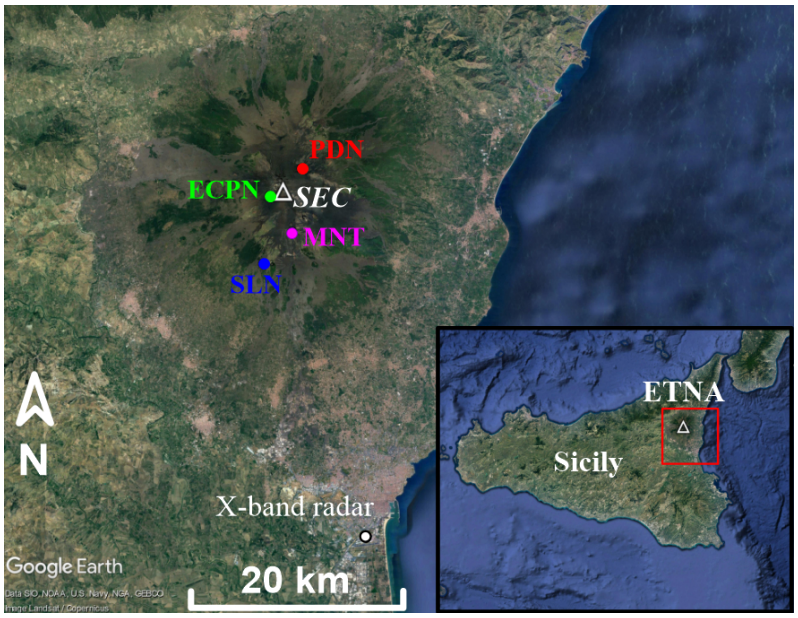

Figure 1: Location of the South East Crater (SEC) and the geophysical and remote sensing systems considered here: gravity stations at Serra La Nave (SLN; blue), La Montagnola station (MNT; purple) and Pizzi Deneri(PDN; red), the seismic station at Cratere Del Piano (ECPN; green) and the X-band weather radar at the Catania airport.

2.2 Remote sensing

2.2.1 ESPs from satellite

Satellite infrared is used to monitor and track the dispersal of tephra plumes and clouds over large time and space scales. In this work, we used the sensor SEVIRI (Spinning Enhanced Visible and Infrared Imager) onboard the 2nd generation Meteosat (geostationary). It provides 3 x 3 km resolution images over Etna every 15 min. Plume heights are obtained thanks to the Dark Pixel procedure (Prata and Grant, 2001) based on the brightness temperature of the darkest pixel of the plume, which is assumed to be in thermal equilibrium with the surrounding atmosphere. By measuring the cloud transmittance in the thermal infrared, the mass of SO2 and ash and their mean particle sizes are retrieved with the Volcanic Plume Retrieval technique (i.e., VPR described in Pugnaghi et al., 2012, 2016; Guerrieri et al., 2015; Corradini et al., 2016, and reference therein). The main advantage of satellite platforms is their capacity of tracking plumes over distances that are way much larger than any other ground-based remote sensing systems such as Doppler radars and visible cameras (i.e., hundreds of km away from vents). However, it is important to note that, in the thermal infrared, SEVIRI-based estimates mainly correspond to detected particles that are <20 µm (i.e., very fine ash Rose and Durant, 2009).

In addition, the Istituto Nazionale di Geofisica e Volcanologia – Osservatorio Etneo (INGV-OE) led operational surveys of lava flows emitted during all paroxysms using ground-based thermal imagery and the MultiSpectral Imagerer (MSI) onboard of the satellite Sentinel-2. We used lava flow volumes that were made available through the multidisciplinary monitoring reports published by INGV-OE [1].

2.2.2 ESPs from X-band Weather radar

We use data from a weather Doppler radar operating at a wavelength of 3×10^{-2}m (X-band) and located at Catania airport, 30 km away from Etna's summit craters (Fig. 1). The radar scans its surrounding environment at 13 different elevations and provide one complete scan every 10 min Montopoli (2016); Vulpiani et al. (2016). In particular, it is able to observe paroxysmal episodes, including fountaining and tephra plume activity, and can provide estimates of plume height and MER in real time Mereu et al. (2020); Marzano et al. (2020); Freret-Lorgeril et al. (2021). In the frame of this work, we applied the Mass Continuity approach (MCA) to derive the Total Erupted Mass (TEM) from the radar data Marzano et al. (2020). This technique is based on the mass conservation equations, by considering the mass of tephra that enters and leaves a constrained volume sounded by the radar above the eruptive vents of Mt. Etna. One of the main advantages of the radar is its capacity to sound in 3D the eruptive columns emitted during Mt. Etna's paroxysms with a good time resolution, independently of weather conditions Freret-Lorgeril et al. (2021); Mereu et al. (2020).

[1] https://www.ct.ingv.it/index.php/monitoraggio-e-sorveglianza/prodotti-del-monitoraggio/bollettini-settimanali-multidisciplinari

2.3 Gravimetry

Two iGravs superconducting gravimeters (SGs) in Mt. Etna's monitoring system are located on the south flank of the vocano, at La Montagnola hut and in the facilities of the Serra La Nave astronomical observatory, 3.5 and 6.5 km away from the summit vents, respectively (Fig. 1). These devices are part of the first permanent mini-array of SGs installed on an active volcano Carbone et al. (2019). SGs provide high-quality data, allowing to track gravity changes as small as 1-2 µgal over a wide range of time scales Carbone et al. (2019). SGs were successfully operating during the February-October 2021 paroxysmal activity. Time series from SGs presented herein are corrected for the effect of earth tide and atmospheric pressure.

In 2020, an Absolute Quantum Gravimeter (AQG-B03), developed by iXblue, was installed in the facilities of the Pizzi Deneri volcanological observatory (PDN in Fig. 1 Antoni-Micollier et al., 2022). Continuous data acquisition with the AQG-B was restarted in May 2021, after a forced winter pause. The AQG-B features an active vibration compensation system, exploiting the data from an onboard broadband seismometer. Hence, the AQG-B is less affected than the SGs at MNT and SLN by ground shaking (Carbone et al., 2019; Antoni-Micollier et al., 2022).

Gravity changes induced by volcanic processes may occur over various timescales (Carbone et al., 2017). Here, we focus on the relatively fast gravity changes occurring before the start of lava fountaining events from Mt. Etna's craters. Strombolian explosions with increasing intensity and frequency occur from several days to a few hours before each paroxysm (Behncke et al., 2014; De Beni et al., 2015; Andronico et al., 2018). This activity produces an increasing seismic activity which is monitored by the INGV-OE in real time. In order to investigate the influence of pre-and syn-eruptive seismic activity on gravity signals, we use tremor data acquired at the Cratere del Piano station (ECPN `http://terremoti.ingv.it/instruments/network/IV`). Our main objective is to compare the gravity signal observed before and during the paroxysms with quantitative observations made by remote sensing systems (i.e., ESPs) and evaluate the capacity of gravimeters to provide insightful information on the paroxysms before they start and/or reach their climactic phases.

2.4 Remote sensing estimates of eruptive source parameters

From February to October 2021, radar and satellite observations were made for 16 and 24 paroxysms, respectively, concomitantly to records of gravity and seismic signals. Overall, maximal ash estimates from satellite range over two orders of magnitude, between 6.8×10^5 and 10.0×10^7 kg with a mean of $1.9 \pm 2.5 \times 10^7$ kg (see Table 1). Ash plumes were tracked over durations comprised between 180 and 1620 min, with a mean of 675 ± 388 min. In addition, mean plume heights retrieved by satellite are between 5 and 13 km (a.s.l.) with an overall mean of 9.4 ± 2.2 km (a.s.l.), typical of Etna's paroxysms (Scollo et al., 2014; Calvari et al., 2018). It is important to note that satellite durations are much longer than those derived by X-band radar (presented below). This is because the sensor captures the plume dispersal of very fine ash up to several hundreds of km away from vent (even after the end of paroxysms), while the radar detection limit is 80 km from its location (Vulpiani et al., 2016; Marzano et al., 2020).

Over 16 paroxysms, weather radar-based values of TEM range between 2.3×10^7 and 3.7×10^9 kg for eruption durations between 50 and 190 min (mean of 97 ± 37 min) (Table 1). This leads to MERs being comprised between 7.7×10^3 and 3.7×10^5 kg/s. These values are coherent with relatively weak paroxysmal activity at Mt. Etna having radar-based MERs in the order of 10^4 to 10^5 kg/s (during the 2011-2013 paroxysmal sequence Freret-Lorgeril et al., 2021).

Finally, bulk lava volumes obtained after each paroxysm by Sentinel-2-MSI imagery are comprised between 0.3and4.0Ö10^6 m^3 with an average of $1.7 \pm 1.2 \times 10^6$ m^3. In order to compute the total mass of lava and pyroclasts emitted for each paroxysms, we converted the lava volume in Dense Rock Equivalent values using the estimates provided by Andronico et al. (2018) and references therein. Considering a magma density of 2700 kg/m^3, the lava mass reported in Table 1 are obtained. Summing the lava masses with weather radar estimates provides total mass of lava and detected tephra comprised between 6.71×10^8 and 9.62×10^9 kg with a mean of $4.71 \pm 2.92 \times 10^9$ kg.

Table 1: Eruptive source parameters retrieved by remote sensing techniques for the various paroxysms of 2021 considered in this work. Lava volumes are reported in weekly multidisciplinary monitoring bulletins provided by INGV-OE (see text).

	Satellite estimates			X-Band radar estimates					
date	**Duration (min)**	**Mean plume height (km a.s.l)**	**Max mass (kg)**	**Duration (min)**	**TEM (kg)**	**MER (kg s^{-1})**	**Lava volumes (× 10^6 m^3)**	**Lava mass (kg)**	**Lava + Tephra mass (kg)**
16/02	**240**	9.5	8.8×10^6	100	5.1×10^8	8.5×10^4	2.6	5.62×10^9	6.12×10^9
18/02	**255**	8.0	4.1×10^6	70	2.5×10^8	5.8×10^4	4.0	8.64×10^9	8.89×10^9
19/02	**915**	10.0	1.2×10^7	100	2.9×10^8	4.8×10^4	4.0	8.64×10^9	8.93×10^9
21/02	**855**	11.0	8.0×10^6	/	/	/	2.9	6.26×10^9	/
23/02	**615**	11.0	1.3×10^7	70	3.1×10^9	7.4×10^5	3.0	6.48×10^9	9.62×10^9
24/02	**735**	11.0	7.9×10^6	150	3.4×10^8	3.8×10^4	2.6	5.62×10^9	5.95×10^9
28/02	**930**	10.0	1.7×10^7	100	2.5×10^9	4.2×10^5	1.7	3.67×10^9	6.17×10^9
02/03	**690**	8.0	3.7×10^6	/	/	/	3.8	8.21×10^9	/
04/03	**1455**	11.0	9.7×10^6	110	5.8×10^8	8.8×10^4	1.1	2.38×10^9	2.96×10^9
07/03	**735**	10.5	2.1×10^7	70	1.4×10^8	3.3×10^4	0.9	1.94×10^9	3.36×10^9
10/03	**765**	9.0	5.2×10^7	190	5.8×10^8	5.1×10^5	1.0	2.16×10^9	2.74×10^9
12/03	**1215**	10.5	1.9×10^7	/	/	/	1.0	2.16×10^9	/
15/03	**195**	5.0	2.2×10^7	/	/	/	1.1	2.38×10^9	/
17/03	**405**	5.0	7.8×10^6	/	/	/	0.9	1.94×10^9	/
19/03	**600**	10.0	1.0×10^8	/	/	/	0.5	1.08×10^9	/
24/03	**1065**	5.0	2.2×10^7	/	/	/	1.6	3.46×10^9	/
01/04	**1620**	9.0	3.7×10^6	/	/	/	1.4	3.02×10^9	/
14/06	**180**	5.3	6.8×10^5	50	2.3×10^7	7.7×10^3	0.3	0.65×10^9	6.71×10^8
19/06	**315**	10.4	4.3×10^6	60	5.9×10^7	1.6×10^4	/	/	/
20/06	**495**	10.2	5.9×10^6	100	1.6×10^8	2.7×10^4	/	/	/
23/06b	**270**	11.1	5.5×10^6	60	5.7×10^7	1.6×10^4	1.1	2.38×10^9	2.38×10^9
24/06	**375**	11.4	5.5×10^6	80	4.2×10^7	8.8×10^3	0.8	1.73×10^9	1.73×10^9
21/09	**585**	10.4	1.4×10^7	100	6.8×10^8	1.1×10^5	0.7	1.51×10^9	1.51×10^9
23/10	**690**	13.0	8.6×10^7	140	3.1×10^9	3.7×10^5	0.5	1.08×10^9	1.08×10^9

2.5 Gravity observations

2.5.1 Gravity changes observed with the iGrav SGs

Between mid-December 2020 and mid-February 2021, strombolian activity of variable intensity interspersed with paroxysmal episodes occurred from the summit craters of Etna (Calvari et al., 2022). During this period, the amplitude of the volcanic tremor recorded at ECPN was already at high levels and it started to further increase since February 15th (Fig.2). During the February sequence of lava fountains, the time series from both SLN and MNT display sharp positive changes in

correspondence to each paroxysm. As reported in Carbone et al. (2019), the peaks in the time series from the two iGravs in Fig. 2 represent the instrumental response of the gravimeters to inertial accelerations, during phases of high volcanic tremor and thus they do not reflect actual changes of the local gravity field.

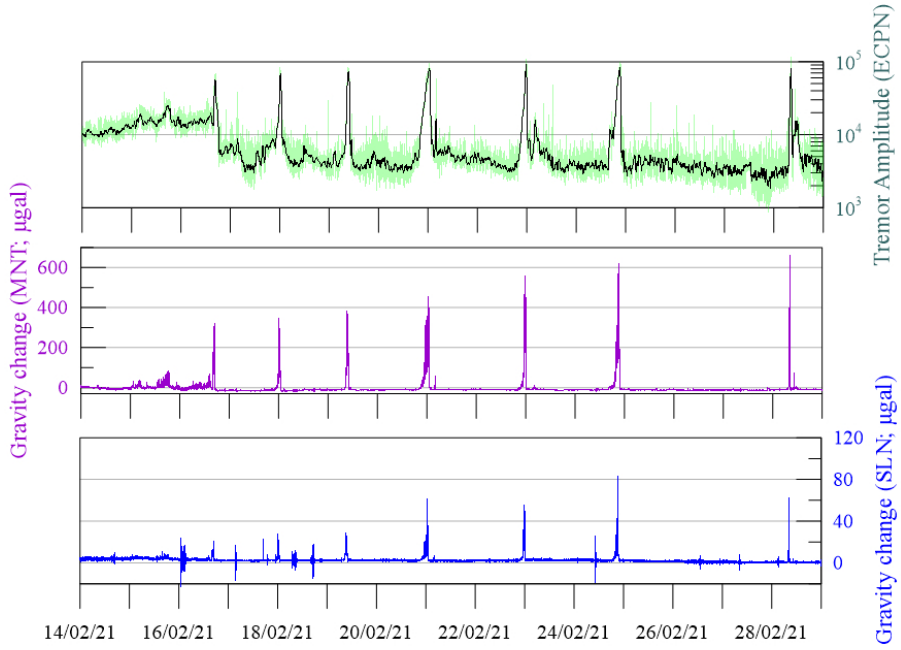

Figure 2: Top panel: February 2021 time series of tremor amplitude (green line; the black line indicates a running average with a 30 min-long time window). Middle and bottom panels: gravity signals from the two iGrav SGs located at La Montagnola station (MNT; purple line) and at Serra La Nave (SLN; Blue line).

A closer inspection on short time windows before each paroxysmal event highlights interesting features of the gravity signals (Fig. 3 and 4). As shown by Carbone et al. (2015), gravity decreases may develop during the last hours before the onset of fountaining episodes at Mt. Etna, corresponding to rapid underground mass redistributions. The results obtained by Carbone et al. (2015) were based on data from a gravimeter installed at a very close distance (< 1 km) from the active crater. Despite they are installed at farther distances from the SEC, small gravity decreases can be observed also in the time series from MNT and SLN before some of the 2021 lava fountains (Figs. 3 and 4), thanks to the high precision of SGs. Interestingly, these decreases occurred during periods when the level of the tremor was flat or only slightly increasing. During February to March 2021, the gravity signal from MNT was very noisy, even during intra-eruptive phases, implying that the pre-eruptive gravity decreases were mostly recognized in the signal from SLN (see Fig. 3).

In most cases, they have an amplitude of less than 1 μGal, start 200 to 2000 min before the fountaining event and end when the paroxysmal activity begins (Figs. 3 and 4) (Table 2). During the later phase of the fountaining sequence, the general quality of the MNT signal improves, probably due to a lower amplitude of the volcanic tremor (top charts of Figs. 3 and 4). It is thus possible to clearly recognize the small pre-eruptive gravity decreases in the signals from both SLN and MNT (Fig. 4). It is worth mentioning that, in some cases, the gravity decrease seems to

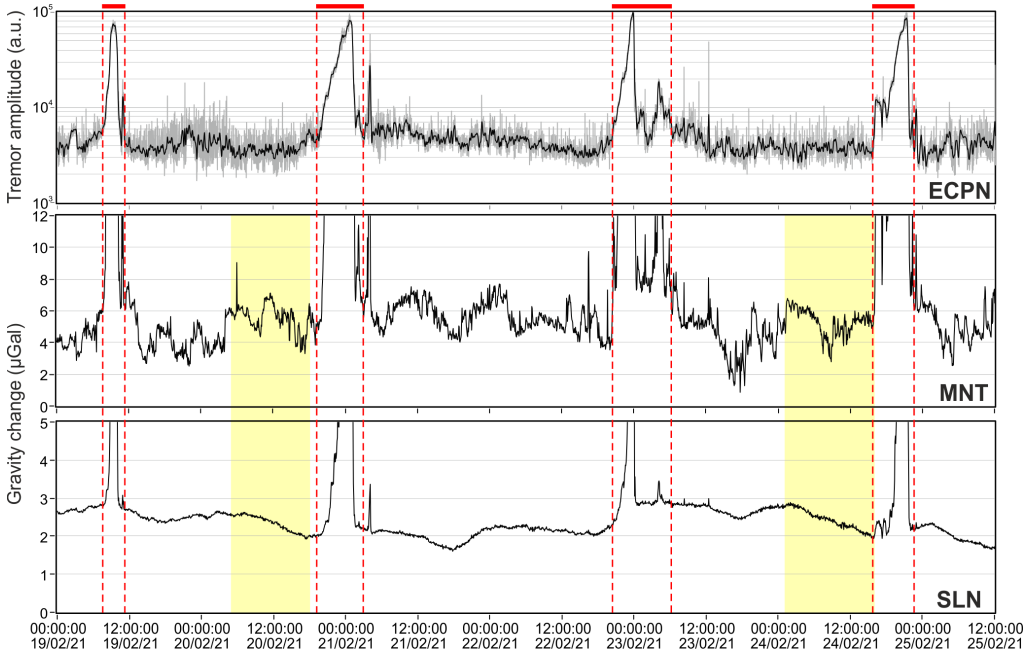

Figure 3: Time series of tremor amplitude (ECPN; top panel) and gravity changes at SLN and MNT (bottom and middle panels) between the 19 and 25 February 2021. Red dashed lines mark start/end of paroxysmal episodes. Yellow areas indicate phases of gravity decreases observed by both iGravs.

end hours before the start of the paroxysmal activity (e.g., gravity change before the fountaining event of 16/06; Fig. 4) and that sometimes no gravity decrease can be detected before a lava fountain (e.g., events of 17-18/06; Fig. 4). In Fig. 4 we also marked (orange area) a gravity decrease which occurred before the onset of Strombolian, rather than fountaining, activity.

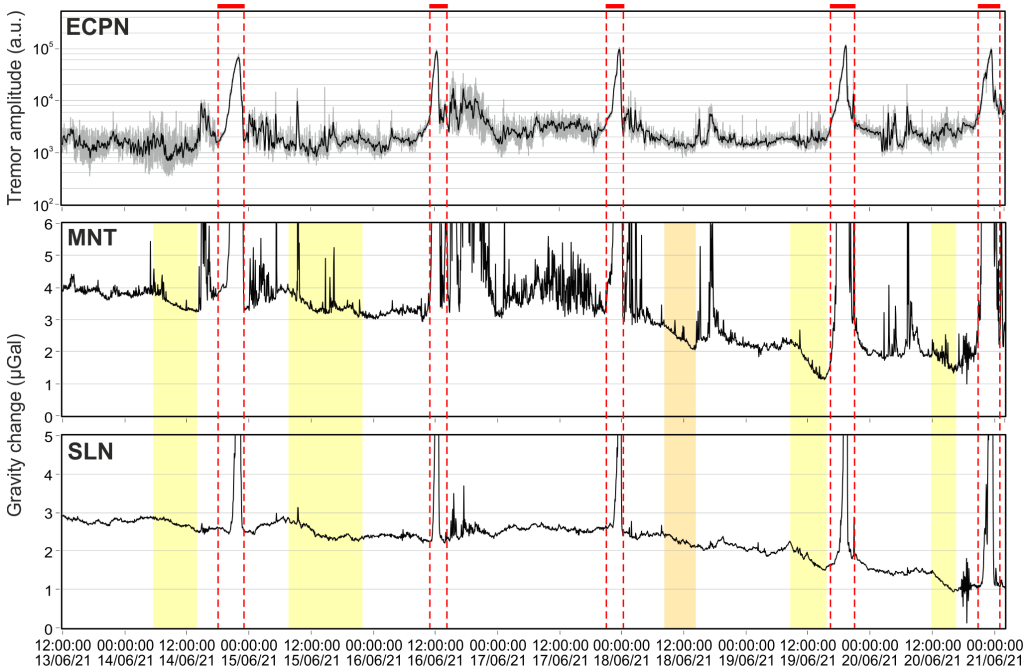

Figure 4: Same as Fig. 3, but for the 13-21 June period. The orange strip indicate a gravity decrease which occurred prior to Strombolian, rather than fountaining, activity.

Table 2: Characteristics of gravity signals observed in the period between February and October 2021. Δg: amplitude of the gravity decreases (μGal); Δt: duration of the decrease (min). NI: Not identifiable

	SLN (5 min avg.)		MNT (5 min avg.)			
date	**Δg (μgal)**	**rate (μgal/day)**	**Δg (μgal)**	**rate (μgal/day)**	**Decrease Δt (min)**	**Time before paroxysm (min)**
16/02	NI		NI		/	/
18/02	0.44	-1.47	2.00	-6.70	430	1100
19/02	NI		NI		/	/
21/02	0.67	-1.32	2.70	-5.33	730	1000
23/02	0.16	-0.23	1.40	-2.08	970	1170
24/02	0.80	-1.37	1.50	-5.83	840	1046
28/02	0.25	-1.89	2.00	-15.16	1030	1584
02/03	NI		NI		/	/
04/03	0.64	-2.67	1.00	-4.17	345	1335
07/03	0.27	-0.81	0.50	-1.5	480	1351
10/03	0.70	-1.05	1.20	-1.8	960	1415
12/03	0.77	-1.23	1.40	-2.24	800	1520
15/03	0.72	-1.12	1.10	-1.71	925	1137
17/03	0.3	-1.31	0.60	-2.62	330	750
19/03	MISSING DATA		NI		/	/
24/03	NI		NI		/	/
01/04	NI		NI		/	/
14/06	0.33	-1.01	NI		470	915
19/06	0.60	-2.4	1.20	-4.8	360	587
20/06	0.60	-1.96	1.00	-3.27	440	840
23/06	NI		NI		/	/
24/06	0.32	-1.61	0.70	-3.54	285	450
21/09	NI		NI		/	/
23/10	NI		NI		/	/

2.5.2 Data from the AQG-B gravimeter

At the end of May 2021, continuous data acquisition with AQG-B03 at PDN (D2.4, D3.6 and Antoni-Micollier et al., 2022) was re-established, after a forced 5-month interruption. The latter was due to issues with the hybrid power supply system of the gravimeter (D3.4), which occurred during the period when the installation site is not reachable (usually, between December and March, due to the snow cover). The gravity time series produced by AQG-B03 in 2021 encompasses nearly 40 lava fountaining events. For 7 of these paroxysms remote sensing observations are available. The AQG-B features a lower precision than iGrav SGs, implying that data from the AQG-B must be averaged over periods longer than 1 h to attain a sensitivity of 1-2 μGal (Antoni-Micollier et al., 2022). That makes it difficult to detect the small gravity decreases expected to occur before each paroxysm (Figs. 3 and 4).

However, the AQG-B is fitted with an active vibration compensation system (Ménoret et al., 2018) and it is thus less affected than iGravs by strong ground shacking during the eruptive phases. Thus, the AQG-B has the potential to spot real gravity changes, even during periods when, due to the high tremor amplitude, iGravs display fictitious changes in the average level of the gravity signal, which are driven by inertial forces (Carbone et al., 2019). As shown in Fig. 5, gravity decreases with amplitude of a few microGal were indeed recorded by AQG-B03 before some lava fountains, but they are difficult to recognize, owing to the unfavorable signal-

to-noise ratio. Such changes usually appear during the last 4-5 hours before the beginning of the most energetic eruptive phase (Fig. 5). A comparison with the signal from the iGrav at MNT (Fig. 5) shows that, while the AQG-B cannot detect the very small gravity decrease tracked by the iGrav from more than 12 to a few hours before the start of the climactic phase (yellow area in Fig. 5), the iGrav cannot detect the change spotted by the AQG-B (orange area in Fig. 5), as it mostly occurs under conditions of high tremor amplitude, when instrumental effects are dominant in the signal from the iGrav.

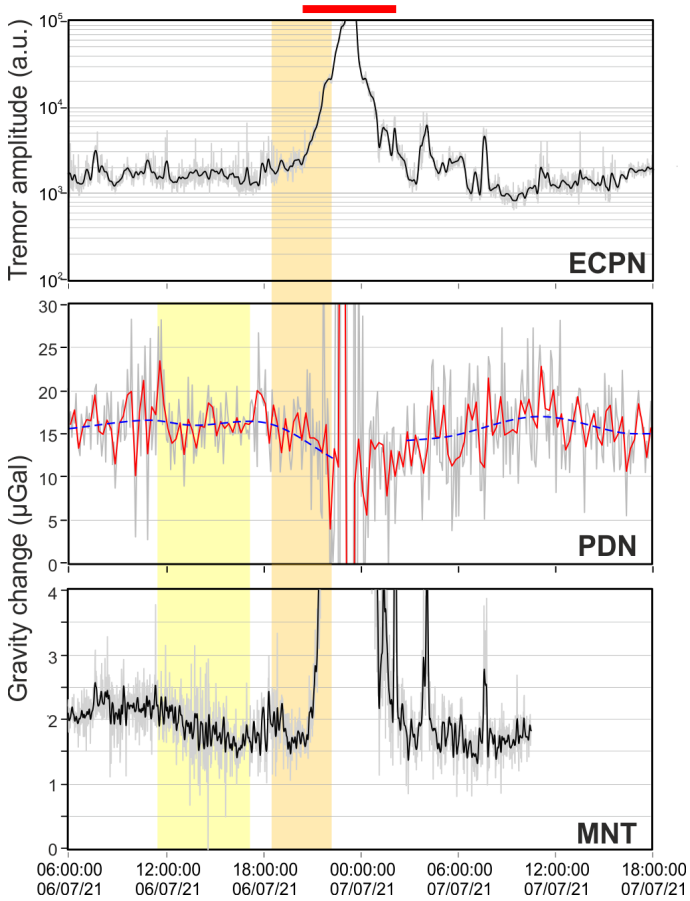

Figure 5: Time series between 06:00 of 06/07 and 18:00 of 07/07/2021. Top: volcanic tremor amplitude calculated using the seismic signal from ECPN station (gray: 1 min data; black: low-pass filter with cutoff freq. = 0.8 mHz). Middle: gravity signal from the AQG-B at PDN (grey: 5 min average; red 15 min average; dashed blue: low-pass filter with cutoff freq. = 33 μHz). Bottom: gravity signal from the iGrav at MNT (grey: 10 sec data; black: low-pass filter with cutoff freq. = 1 mHz). The yellow strip marks the gravity decrease tracked by the iGrav SG, while the orange strip evidences the subsequent change only recognizable in the signal from the AQG-B at PDN. The red thick line in the uppermost part of the figure marks the most energetic phase of the lava fountain.

Given (i) the limited number of fountaining episodes covered by both AQG-B gravity data and remote sensing observations and (ii) the difficulty to establish quantitative features of the short-term gravity changes assessed through the AQG-B prior to lava fountains, in the following we do not use gravity data from this device to perform comparisons with the amounts of erupted material.

2.5.3 Longer-term gravity changes during 2021

Besides the short-term small changes observed in the gravity time series, in correspondence to lava fountain events, the signals from the two iGravs at SLN and MNT and the AQG-B at PDN displayed common longer-term gravity changes in 2021 (see D2.6). One of the most interesting is the gravity decrease which occurred during early June to late July, with an overall amplitude of about 20, 16 and 7 μGal at PDN, MNT and SLN, respectively (Fig. 6).

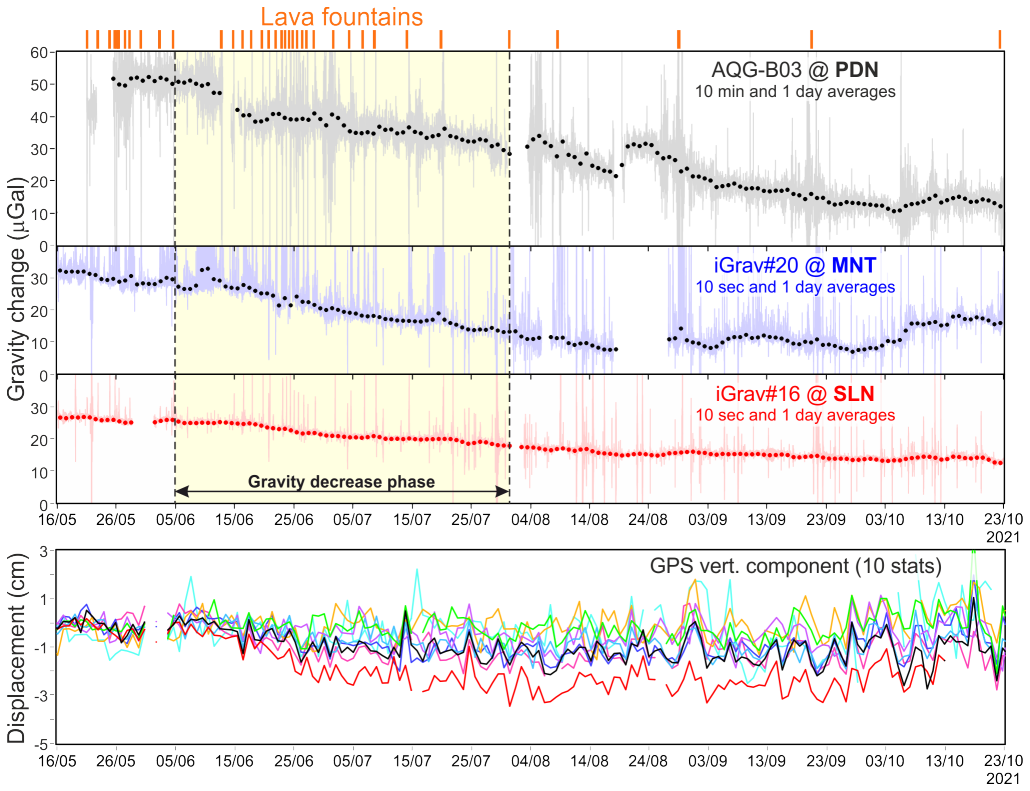

Figure 6: Time series during 16/05 to 23/10/2021. Upper 3 charts: gravity time series from the AQG-B at PDN and the two iGravs at MNT and SLN. Data from PDN are averaged over 10 min (grey curve) and 1 day (black dots). Data from MNT and SLN are averaged over 10 sec (blue and red curves, respectively) and 1 day (black and red dots, respectively). Bottom chart: GPS time series (vertical component) recorded at 10 stations of the network managed by INGV-OE.

During the period when this gravity decrease developed, (i) 22 lava fountain events took place (see marks in the upper part of Fig. 6) and (ii) overall deflation of the volcanic edifice was detected through GNSS data (bottom chart of Fig. 6). A joint inversion of the gravity (3 stations) and GNSS (20 stations) data across the 05/06 - 31/07 period was performed using a convergent Pattern Search Algorithm (Cannavo' et al., 2019). Results indicate that the source body, located beneath the summit craters, at depth of 2-3 km b.s.l., underwent a volume and mass reduction of about 2×10^6 m^3 and $1.4 \times 10^1 1$ kg, respectively. The mass change imaged by gravity largely exceeds the volume change resulting from the joint inversion, for any reasonable density of the material extracted from the source body. That could indicate that, beside loosing magma to the eruptions, gas-to-magma substitution occurred within the source reservoir. In other words, gas exsolution and expansion led to a source volume reduction much less than the real volume of magma lost

from the source reservoir and to a mass decrease much larger than expected from deformation data only. Indeed, if one considers the average volume of lava emitted by each fountaining episode (1.7×10^6 m^3; Section 2.2.1), it is clear that the volume change resulting from the joint inversion is much less that the volume emitted by the 22 lava fountains during early June to late July.

These results clearly show that only through joint analysis of deformation and gravity data it is possible to assess a full picture of the processes behind phases of volcano inflation or deflation. In particular, the availability of continuous gravity data from precise and stable (i.e., driftless) instruments allows to track even small changes (a few μGal) over relatively long time-scales ($>$ 1 month), implying that joint inversion of gravity and deformation data could be routinely performed for mid-to-short-term hazard analysis.

2.6 Comparison between remote sensing data and gravity observations

In this section we compare remote sensing estimates (Section 2.2.1 and Table 1) with information retrieved from the gravity signals recorded in 2021 (Table 2). Since the amplitude of the changes observed by the iGrav at SLN are very close to the detection limit of the instrument, we focus on gravity data from MNT, which, being nearer to the active structures, is affected by stronger (and more significant) volcano-related gravity changes. As shown in Fig. 7, the amplitude of the gravity decreases observed at MNT is roughly but significantly correlated with both the emitted mass of lava (Fig 7a) and the total mass of tephra and lava (Fig. 7b). Conversely, no correlation is found between the amplitude of the gravity decreases and the maximum estimates of ash mass from satellite (Fig 7c).

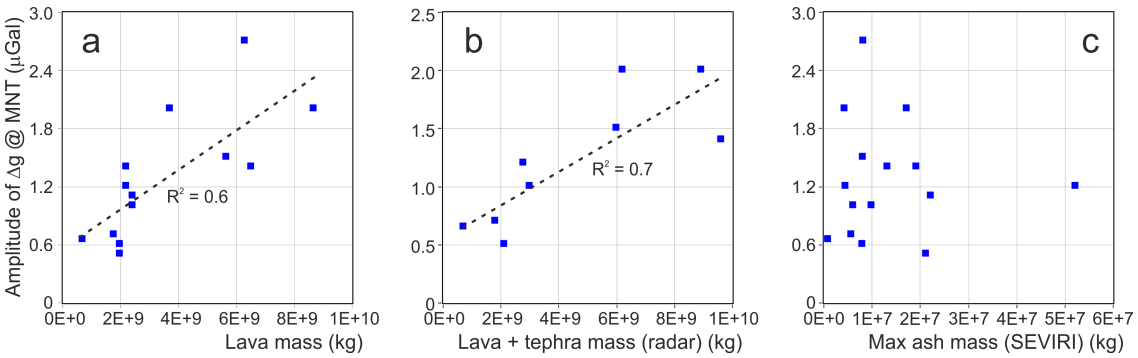

Figure 7: Amplitude of the gravity decreases observed at MNT before the climactic phase of lava fountain events, plotted against (a) the mass of emitted lava flows, (b) the mass of lava plus the radar-estimated mass of pyroclasts, (c) the maximal ash mass observed by satellite infrared (see Tables 1 and 2)

Taking into account the durations over which each gravity decrease occurs does not improve the coupling with erupted masses retrieved through remote-sensing methods. Indeed, if the average rate of the gravity changes is considered, rather than their amplitude, the correlation with erupted masses worsens, as shown in Fig. 8. This is probably due to the difficulty in precisely and objectively defining the starting time of the low-rate gravity changes against the background noise (the changes usually develop under high tremor conditions).

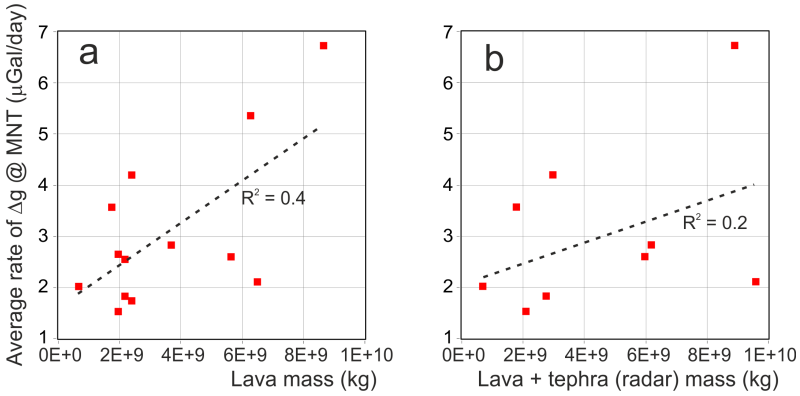

Figure 8: Average rate of the gravity decreases observed at MNT before the climactic phase of lava fountain events, plotted against (a) the mass of emitted lava flows, (b) the mass of lava plus the radar-estimated mass of pyroclasts (see Tables 1 and 2)

In order to properly interpret the results shown in Fig. 7, one should consider the characteristics and limits of the remote sensing data jointly analyzed with gravity observations. For example, we use satellite infrared (SEVIRI sensor) to track the mass of ash and gas in the volcanic plume. Nevertheless, only the mass of SO_2 and very fine ash (particles with size <20 μm) is detected by measuring transmittance in the thermal infrared. Hence, also considering that water vapor, rather than SO_2, is the most abundant gas released during explosive events, this technique provides only a very partial picture of the emitted amounts. That could explain the lack of correlation with the gravity data. The weather radar detects tephra from fine ash (<25 μm) up to lapilli (≤ 64 mm) (Marzano et al., 2011; Freret-Lorgeril et al., 2021) and, once the information it provides on the mass of tephra is summed up with the mass of emitted lava retrieved from ground-based and satellite thermal imagery, a more reliable assessment of the total erupted mass is obtained.

The loose correlation with the amplitude of the observed gravity decreases may thus indicate the existence of an indirect link between the pre-eruptive underground mass change and the amount of the erupted mass. Relying on the hypothesis that the gravity decreases reflect gas-to-magma substitution in the source volume (Carbone et al., 2015), the couplings presented in Fig. 7 suggest a direct relationship between amounts of driving gas and emitted mass.

2.7 Perspective and future applications

Within the limits of the available data, that were discussed in the previous sections, we present the first ever attempt to investigate possible links between pre-fountaining short-term gravity changes and amount of mass emitted by the fountaining events. Our results show that a weak direct relationship does exists between amplitude of the gravity (i.e., underground mass) decreases, taking place during the last 6-24 hours before the climactic phase of the fountaining events, and mass of erupted tephra and lava. Continuous gravity data thus have the potential not only to allow early identification of energetic explosive episodes, but could also provide a first-order estimate of the amount of volatiles accumulated at depth before the breakout of the fountaining event.

Nonetheless, further effort is needed to make gravimetry a core component of

short-term volcano hazard assessment. iGrav SGs feature very high precision and long-term stability, allowing to detect even very small changes (on the order of 1 μGal or less), occurring over a wide range of time-scales (few minutes – several months). However, they are expensive and power-hungry, implying that it is not possible to deploy dense arrays of iGravs in close vicinity to the active structures of tall volcanoes. Furthermore, the signal from iGravs is affected by ground shaking from strong volcanic tremor, implying that it is not possible to obtain meaningful gravity data during the most energetic phases of explosive events. The AQG-B is less affected by ground shaking, but features a lower precision than iGravs and cannot detect fast (occurring over a few hours) and small (few μGal, or less) gravity changes. Ideally, an array of devices less expensive and power-hungry than the iGrav and AQG-B and providing continuous gravity data with adequate signal-to-noise ratio should be deployed as close as possible to the active craters, in order to characterize the pre-fountaining changes with a sufficient level of reliability and space resolution. MEMS gravimeters could fulfill this need (Carbone et al., 2020), but require further development to attain the required characteristics. Alternatively, old refurbished L & R spring gravimeters, which come at a much lower price than new instruments, can be successfully used to continuously track volcano-related changes (Carbone et al., 2015, 2017). It is important to remind that the reference provided by more stable and precise instruments is key to fully exploit the potential of devices providing lower-quality data (i.e., the NEWTON-g's concept of "gravity imager").

3 Development of fundamental modelling tools

Mehdi Nikkhoo and Eleonora Rivalta

3.1 Point-source and finite-source modelling tools

Pressurization of a magma chamber due to new magmatic intrusions leads to deformation and mass redistribution throughout the host rocks. The new intrusion mass and host rock deformations cause gravity changes. The total gravity change, δg, at a surface gravity station (triangle in Fig. 9), is the sum of contributions from vertical displacement, u_v, of the station (free-air effect, Δg_{FA}), displaced rock mass immediately below the station (similar to the Bouguer effect, Δg_{SM}), density change due to volumetric strain throughout the host rocks ($\Delta g_{\epsilon_{\mathrm{kk}}}$), displaced rock mass at the chamber walls ($\Delta g_{\delta \mathrm{V_c}}$) and, last but not least, the new intrusion mass ($\Delta g_{\Delta \mathrm{M}}$). Thus, we can write:

$$\delta g = \Delta g_{\mathrm{FA}} + \Delta g_{\mathrm{SM}} + \Delta g_{\epsilon_{\mathrm{kk}}} + \Delta g_{\delta \mathrm{V_c}} + \Delta g_{\Delta \mathrm{M}} \tag{1}$$

We refer to the terms Δg_{FA}, Δg_{SM}, $\Delta g_{\epsilon_{\mathrm{kk}}}$ and $\Delta g_{\delta \mathrm{V_c}}$ as 'deformation-induced' gravity changes because they all arise from the deformation of the host rocks caused by the chamber pressurization. In order to constrain the intrusion mass from gravity data these deformation-induced gravity changes must be somehow determined.

Deformation-induced gravity changes may be substantial or even larger than the contribution due to intrusion mass. While Δg_{FA} and Δg_{SM} can be calculated directly from observations (vertical displacement measurements, e.g. from level-

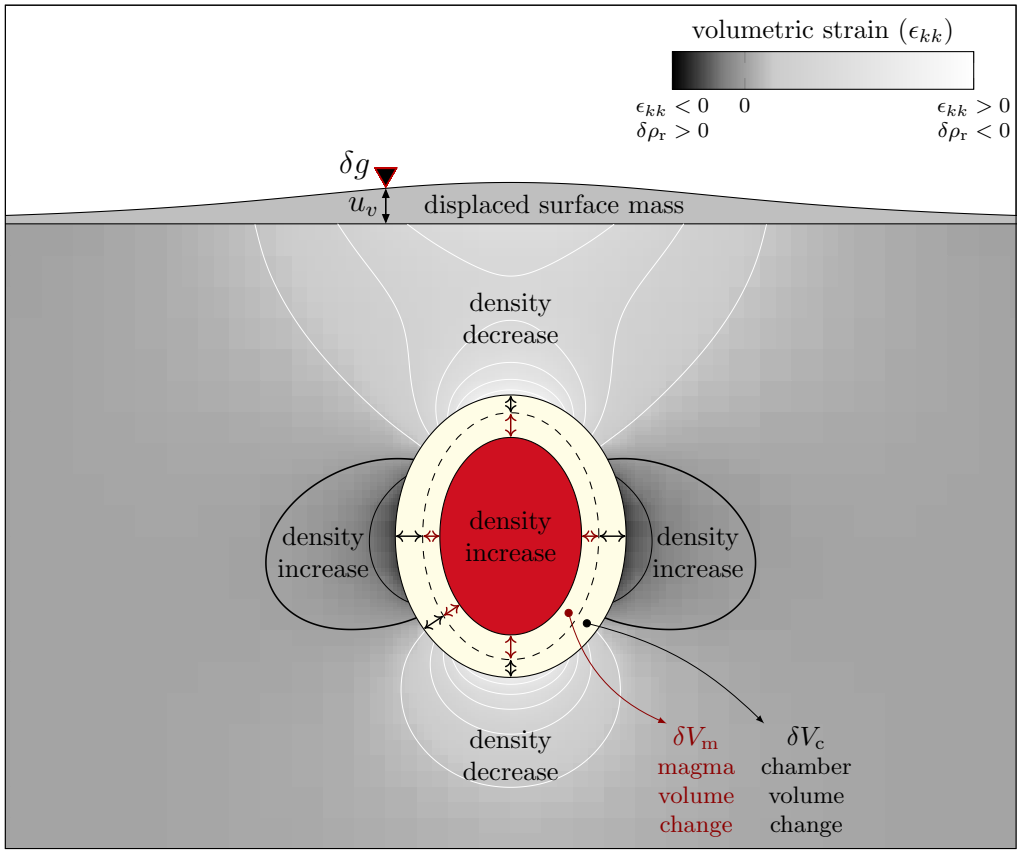

Figure 9: Deformation-induced gravity change contributions due to intrusion of magmatic fluids into, and pressurization of, a pre-existing magma chamber. Figure from Nikkhoo and Rivalta (2022a).

ling or GNSS), the contributions $\Delta g_{\epsilon_{kk}}$ and $\Delta g_{\delta V_c}$ can only be calculated from a deformation model.

In the framework of NEWTON-g, the GFZ team developed two solutions that can be used to calculate the deformation-induced gravity changes caused by triaxial volumetric sources. The first solution (Nikkhoo and Rivalta, 2022a) provides the gravity change contributions associated with the point Compound Dislocation Model (point CDM, Figure 10a) after Nikkhoo et al. (2017). The point CDM is an analytical point-source model that can be applied to sources with depth to the center, d_C, several times larger than the semi-major-axis, a_C. The second solution (Nikkhoo and Rivalta, 2022b), called the finite Ellipsoidal Cavity Model (finite ECM, Figure 10b) provides both the deformation and the deformation-induced gravity changes for a uniformly-pressurized finite triaxial ellipsoid. The finite ECM is a quasi-analytical finite-source model, which can be applied to moderately-deep to shallow sources with $d_C/a_C \gtrsim 2$.

The most critical novelty regarding the newly developed models is that they allow to compute rapidly the contribution $\Delta g_{\epsilon_{kk}}$ for generic triaxial sources. The finite source solution represents a novelty also in terms of deformation. Both models were carefully validated against the Trasatti and Bonafede (2008) numerical solutions, which are based on the Finite Element Method (FEM), as summarised in Fig. 11, and several hundreds Boundary Element Models (BEM) set up ad-hoc for these tests.

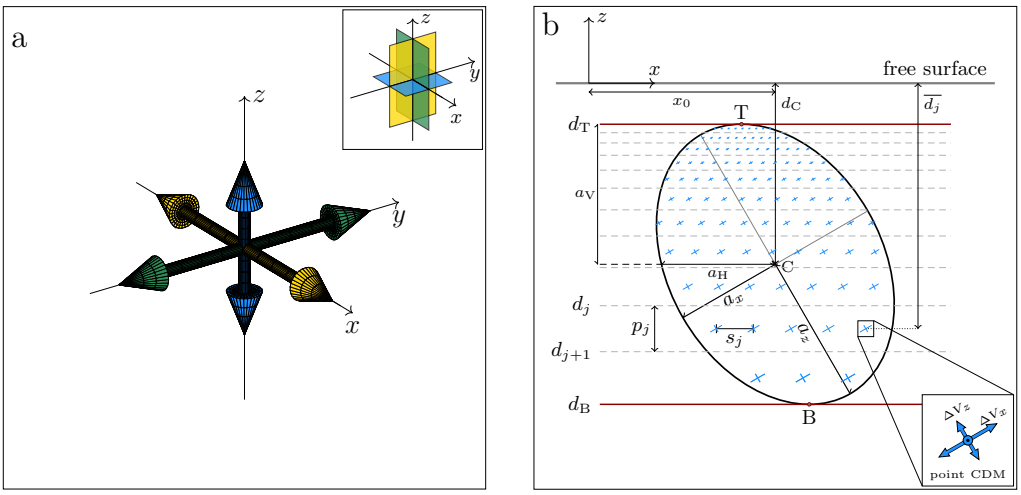

Figure 10: Schematic representation of the newly developed source models. a) The point CDM (inset is the CDM, with three mutually orthogonal dislocations, the point CDM is the corresponding point source). These models were developed by Nikkhoo et al. (2017); in the framework of NEWTON-g, the GFZ team developed analytical solutions for the corresponding gravity changes (Nikkhoo and Rivalta, 2022a). b) The finite ECM, composed of a set of point CDMs distributed according to a depth-dependent spacing scheme (Nikkhoo and Rivalta, 2022b).

A consolidated procedure to infer the mass change of a pressurized magma body from deformation data and gravity changes involves:

1. inverting deformation data for the chamber location, (x_C, y_C, d_C);
2. calculating $\Delta g_{\Delta M}$ from δg by removing all other contributions in equation 1;
3. calculating ΔM from Newton's law,

$$\Delta M = \frac{|\Delta r|^3}{G d_C} \Delta g_{\Delta M}, \tag{2}$$

where $|\Delta r|$ is the distance of the surface gravity station to the center of the chamber.

From the volume change, which can also be constrained from deformation data, and ΔM, the density of the intrusion can be estimated. This requires an estimate of the compressibility of the magma previously contained in the chamber (see D4.3).

The newly developed solutions provide the means to apply the aforementioned procedure to sources of a wider range of shapes than previously possible. Indeed, failing to account for the triaxial source geometry of most magma bodies biases the inferred source parameters. The lack of an analytical solution for the gravity changes due to the pressurization of triaxial deformation sources was a recognized gap in volcano geodesy (Segall, 2010). Especially the term $\Delta g_{\epsilon_{kk}}$ (the contribution due to induced volumetric strains), which have complex patterns even for simple idealized reservoir or intrusion geometries, could not be calculated through any available analytical solution. Note that the term $\Delta g_{\epsilon_{kk}}$ can be calculated through numerical methods such as the FEM (Currenti et al., 2007; Trasatti and Bonafede,

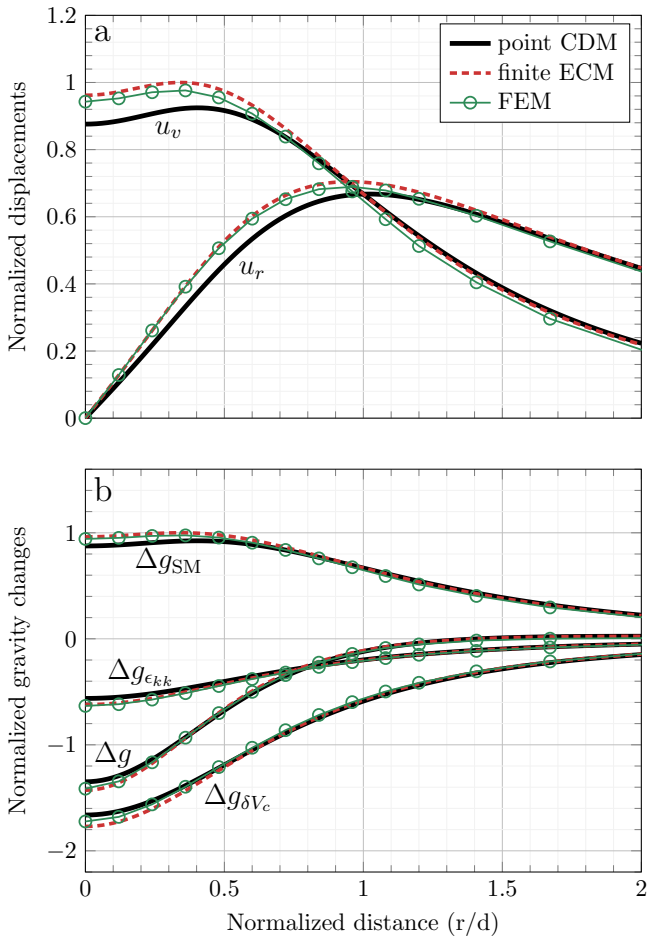

Figure 11: Validation against solutions by Trasatti and Bonafede (2008) for a vertically elongated spheroidal cavity (semi-major axis is 1850 m, semi-minor axis is 740 m, depth to the centre is 5000 m). Top: vertical (u_v) and radial (u_r) surface displacements, bottom: gravity changes. Note that $\Delta g = \delta g - \Delta g_{\mathrm{FA}}$. Figure from Nikkhoo and Rivalta (2022a).

2008; Currenti, 2014, 2018) or BEM. These methods can account for host rock heterogeneities and additional source shape complexities. However, applying these techniques to joint inversions of surface deformations and gravity changes is very challenging (see Section 3.3).

The MATLAB codes associated to our newly developed models are open source and can be downloaded, together with examples, from the website `https://www.volcanodeformation.com`.

3.2 Development of new joint inversion concept

As mentioned in Section 3.1, deformation and gravity changes have been used together to infer mass change associated with magmatic intrusions. More procedures have been proposed where the ground displacements and the gravity changes are inverted jointly. All these approaches follow the consolidated procedure to apply the free air-correction to the data prior to the inversion.

In a manuscript currently in preparation, we propose to change the paradigm for joint inversions of deformation data and gravity changes; this paradigm change revolves around how and at which stage the 'free-air' contribution is accounted for,

and the implications for elevation control at gravity benchmarks.

One of the largest terms in equation 1 is generally the free-air contribution:

$$\Delta g_{\mathrm{FA}} = \gamma u_v, \tag{3}$$

where γ is the free-air gradient. Considering an average value of $\gamma = 0.3086\,\mu Gal\,m^{-1}$, for $u_v = 1\,\mathrm{cm}$ we have $\Delta g_{\mathrm{FA}} = 3\,\mu\mathrm{Gal}$. Therefore, the typical uplifts observed at volcanoes, which may reach centimeters to decimeters or, occasionally, even meters, produce substantial free-air contributions. Depending on the technique used to monitor the vertical displacements, the uncertainties associated with the free-air contribution, $\sigma_{\Delta g_{\mathrm{FA}}}$, can also be substantial:

$$\sigma_{\Delta g_{\mathrm{FA}}} = \gamma \sigma_{u_v}, \tag{4}$$

where σ_{u_v} is the uncertainty associated with the vertical displacement. Typical values of a few centimeters for σ_{u_v} lead to $\sigma_{\Delta g_{\mathrm{FA}}} \simeq 10 - 15\,\mu\mathrm{Gal}$, which will propagate onto the corrected/residual gravity changes. This undermines the quality of present-day gravity observations, which can reach sub-μGal accuracy.

If we are interested in retrieving the mass change, it is imperative that deformation measurements are carried out and evaluated together with the gravity changes. If no mass change is involved, any surface gravity change can be attributed to vertical displacement of the surface. In such case, a gravity change measured with $\sigma_{\Delta g} \simeq 0.1\,\mu\mathrm{Gal}$ uncertainty reveals a vertical displacement with uncertainty $\sigma_{u_v} = 0.3\,\mathrm{mm}$. This means that the gravimeter can act as an extremely accurate sensor to measure the vertical displacement of the gravity station. The reason that gravimeters cannot be used for that purpose is that subsurface mass redistribution also contributes to the observed gravity changes.

To address this issue, we avoid applying the free-air correction prior to the inversion. Rather, we let the search scheme find the set of model parameters that fit the best to all surface deformation and gravity change observations (corrected for all the external effects, but the free-air contribution). This way, the free-air effect is accounted for within the model without having to calculate it prior to the inversion. In other words, the free-air effect, and all the other gravity change contributions in equation 1, are constrained simultaneously with the deformation source parameters and intrusion mass.

We apply the new joint inversion approach to the deformation and gravity data from the 1982–1999 inflation period at Long Valley caldera (Figure 12). The available data over this time period consist of campaign gravity measurements, vertical displacements from levelling and horizontal displacements from the EDM. We first apply the new joint inversion approach to all the datasets. All the source parameters are constrained well, as illustrated by the PDFs of the source depth and mass change (Figure 13). We then repeat the inversion using the new approach but excluding the levelling data. Even so, all source parameters are well constrained and compare well with the previous estimates (Figure 14). The modelled gravity changes also fit reasonably well to the observed gravity data (Figure 15). Moreover, the model can predict the vertical displacements at all gravity stations (Figure 16). This example shows that:

1. the new approach can better exploit gravity data to provide constraints on both the sub-surface mass redistribution and surface vertical displacements;

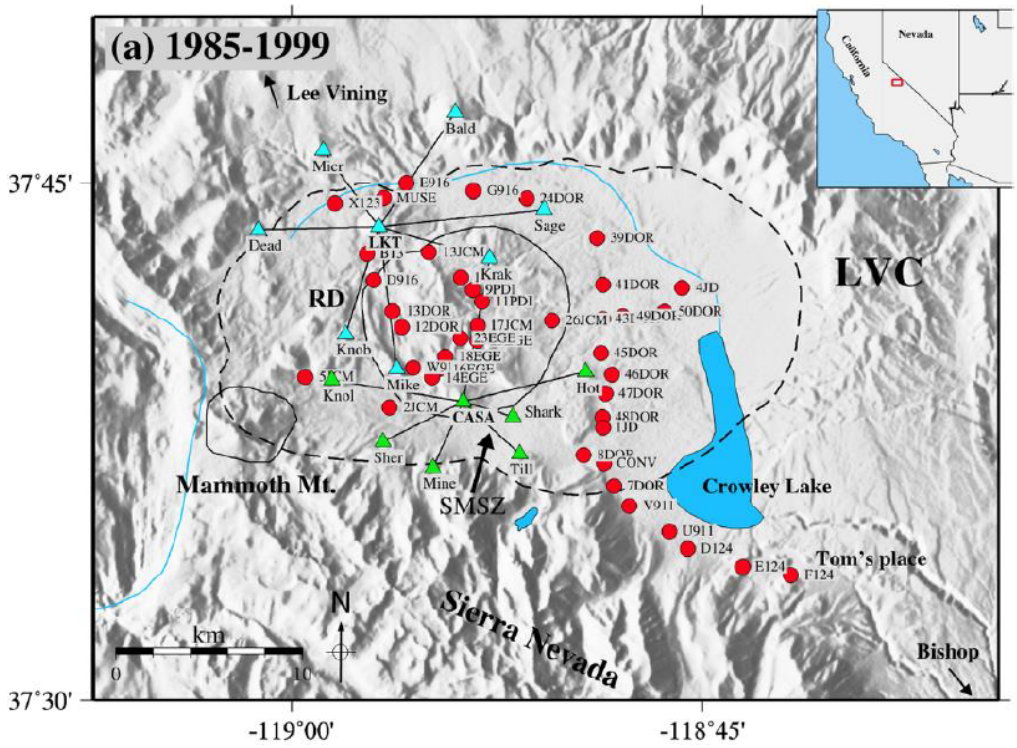

Figure 12: Gravity and levelling (red circles) and EDM (blue triangles) stations at Long Valley caldera. The inner solid line indicates the boundary of the resurgent dome; the outer dashed line indicate the caldera border faults. Figure from Pulvirenti et al. (2021).

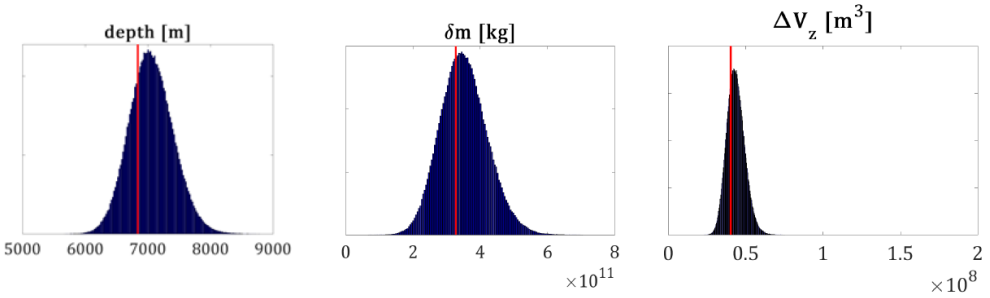

Figure 13: Posterior PDFs for depth, mass change and z-component of potency associated with the joint inversion involving all gravity, levelling and EDM data. The red lines indicate best-fitting solutions.

2. using this new approach we can separate the relative contribution of vertical displacement and mass change to the observed gravity changes;

3. vertical displacement measurements co-located with the gravity benchmark are not a pre-requisite for joint inversions with this approach, in contrast to previous approaches;

4. this approach reduces, at least theoretically, the uncertainties associated with the deformation source parameters and the intrusion mass;

5. this approach shows that gravimeters can also be used to monitoring elevation changes.

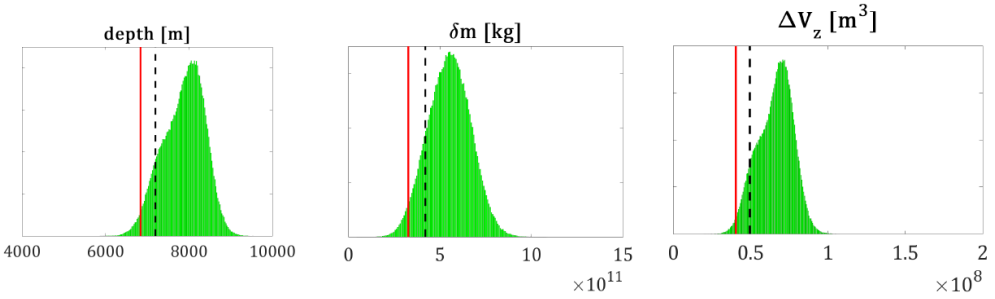

Figure 14: Posterior PDFs for depth, mass change and z-component of potency associated with the joint inversion involving gravity and EDM data only. The dashed lines indicate best-fitting solutions while the red lines indicate best-fitting solutions from figure 13.

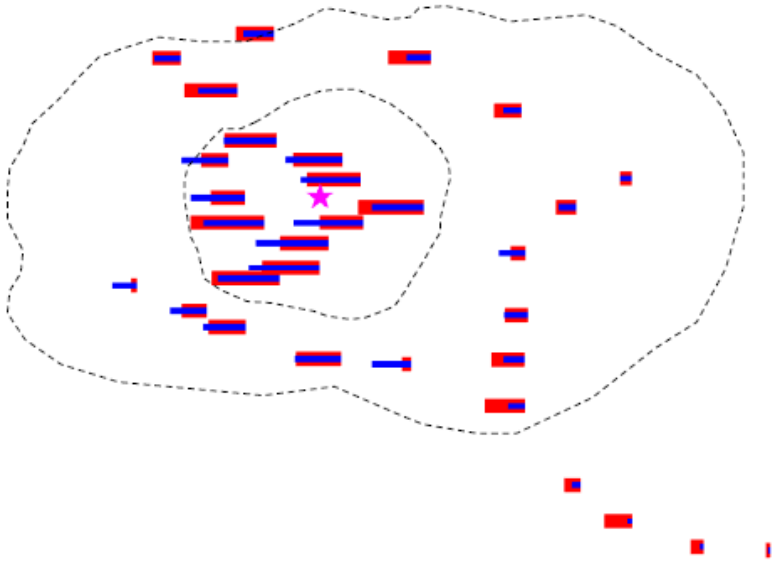

Figure 15: Model fit to the gravity observations. Observed (red) and modelled (blue) gravity changes. The star indicates the inferred source location. The inner dashed line indicates the boundary of the resurgent dome; the outer dashed line indicate the caldera border faults.

More details on how the inversions are done will be included in the manuscript in preparation. In the same paper we will also discuss another main issue omitted here for brevity: the relative weight to be assigned within the inversion procedure to datasets of different nature (here gravity changes, levelling and EDM data).

3.3 Discussion: The added value of analytical solutions for volcano geodesy

By using numerical models such as the finite element method (FEM) it is possible to achieve a more realistic representation of the rheological and geometrical complexities in the earth's crust and the plumbing system of volcanoes. However, analytical or quasi-analytical models retain fundamental importance in crustal deformation studies, due to a number of reasons:

1. Constraining crustal and source complexities, such as the real shape of subsur-

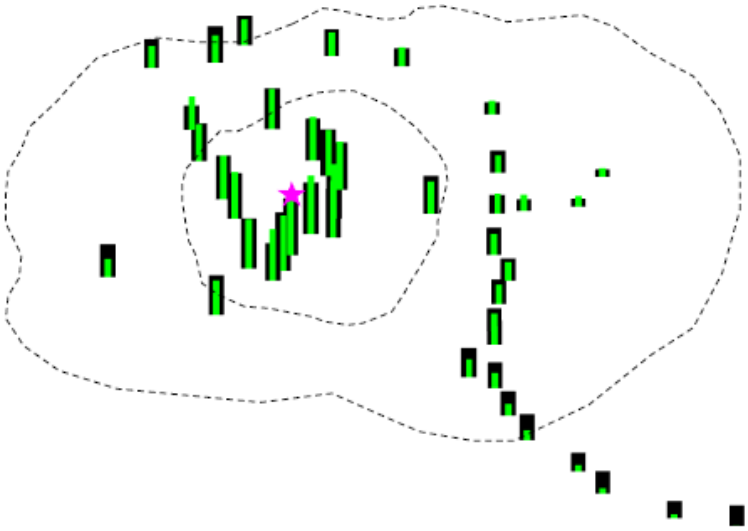

Figure 16: Comparison between predicted (green) and observed (black) vertical displacements. The star indicates the inferred source location.

face layers and their stiffness, as well as the details of the shape of magmatic sources, is not always possible. Also, the rock properties may be difficult to estimate e.g. from seismic measurements, as they may differ from frequency to frequency. Beside the uncertainties related to this lack of knowledge, this means that, with FEM, one may need a dedicated study, not only for every individual volcano, but also for individual events. Indeed, at volcanoes drastic changes are possible in the topography (see the extreme example of caldera collapse at Kilauea in 2018), rheology (e.g. due to the cumulative effects of intrusions or heat transfer), etc. In contrast, analytical models have more 'universal' value and allow for rapid insight into the physics of volcano deformation.

2. Complexities may be many (beside topography we have poroelastic and thermoelastic effects, rock damage, compressibility of the fluids, phase transitions, and more). However, countless studies have shown that specifically for surface deformation modelling, an "effective" medium with average elastic properties works rather well. This is also an advantage, as predictive models (models aimed at predicting the future behavior of a system, as opposed to models aimed only at accurately reproducing data from the past) work better if the number of parameters are reduced to a minimum (Occam's razor).

3. In order to set up the appropriate domain size and mesh for numerical models, they usually need to be benchmarked against analytical solutions. Availability of more complex analytical solutions is of great advantage for this task.

4. While a time frame of two weeks might be acceptable for an 'academic' inversion study of volcano deformation, there are other community needs that require speed and ease of execution. Volcano observatories require source models for real-time or near real-time (tens of minutes to one hour) inference of the parameters of pressurized magma bodies to detect changes in the state of magma chambers or ascending magma pockets, so that these can be communicated to Civil Defence or other authorities, in case of imminent

risk for the population. Indeed, magma propagation and volcano unrest may take place over timescales on the order of a few hours (e.g., Beauducel et al., 2020b, Hreinsdóttir et al., 2014, Aoki, et al., 1999). In spite of the available computational power and sophisticated numerical techniques, for such tasks the volcano-deformation community continues to rely on analytical solutions. The reasons are multiple: simplicity of use in terms of setting up the model and the inversion, ease of interpretation of the results, no need of paying expensive licenses, exportability to different volcanic contexts, or even the same volcano for different events.

5. Systematic analysis of surface displacements during inflation/deflation periods (Bruno et al., 2022, Montgomery-Brown et al., 2015) or magma propagation events where the source migrates rapidly (Beauducel et al., 2020) use analytical solutions in spite of the fact that for some of such cases the volcanoes are well studied and their layering structure is known (e.g. Chiarabba et al., 2004, for Etna and similar studies for other volcanoes) or FEM have already been set up for the volcano.

6. Another fact hinting at the importance of analytical solutions in crustal deformation studies is the fact that many researchers have devoted significant effort (and continue to do so) to develop toolboxes based on analytical point sources (Cannavò 2019, Beauducel et al, 2020a, Bagnardi and Hooper 2018, Battaglia et al, 2013, Trasatti 2022).

7. Process-oriented physical models often use simple analytical solutions to 'predict' the observations expected, taking advantage of their ability to capture the main features of the deformation sources. Again, more flexible analytical or quasi-analytical models can be very helpful in these contexts. Additionally, some 'hybrid' numerical methods include analytical magma chamber models in an otherwise more complex model. The aim is to reduce model parameters whenever possible. Analytical solutions are optimal for this purpose.

Thus, analytical solutions are far from obsolete, and numerical methods such as the FEM, BEM, DEM, etc., may never entirely replace them. Rather, analytical and numerical approaches are complementary and define two end members of a wide range of modeling possibilities, with the optimal technique depending on the specific purpose.

3.4 Additional considerations

1. Deformation-induced gravity changes are important contributions that need to be included in forward and inverse models in order for the calculated gravity changes to be correct and unbiased.

2. For an optimal future exploitation of gravity changes, high-quality deformation monitoring needs to accompany gravity monitoring. In particular, deformation monitoring needs to have high spatial resolution, which is important in order to retrieve correctly the shape of the source, and the same temporal resolution as the gravimeters.

3. With the newly developed tools, all contributions to deformation and gravity changes induced by any pressurized source in the subsurface can now be calculated in a consistent and comprehensive way. This opens the possibility to perform scenario-based modelling.

4 Scenario-based models of gravity changes during lava fountains at Etna

Luigi Passarelli, Eleonora Rivalta, Mehdi Nikkhoo, Costanza Bonadonna

The newly developed modeling tools presented in the previous sections and the other fundamental models previously derived and reported in D4.3 are simple and computationally light tools to build scenario-based synthetic time series of gravity changes for many different volcanic processes. Scenario-based modelling is key for hazard assessment and early warning. However, the limited knowledge of volcanic processes and the inadequacy of the space/time resolution featured by the available deformation and gravity data has so far hindered the development of gravity models specifically tailored for hazard assessment.

These considerations pushed the UNIGE and GFZ teams of NEWTON-g to join forces and develop new and simple physics-based models aimed at producing synthetic time series of gravity changes induced by LFs. We benchmark this models with the gravity changes observed during the 2011 LF episodes at Mt. Etna, still among the best available gravity data through LFs, in spite of having been observed at a single station. We conceived two models: a modification of the classical chamber-conduit model by Okubo (2020) and a new model that simulates the ascent of a batch of gas-rich magma within the volcano edifice as a migrating tensile dislocation. We introduce and implement the two models and discuss their ability to reproduce the observations. Beside the specific applications, both models are flexible and can be adapted to investigate other eruptive processes. They can also produce scenario-based simulations of time series of gravity to be used in probabilistic volcanic hazard assessment.

4.1 Data of Lava Fountains in 2011

Lava fountains (LFs) have been one of the most frequent eruptive manifestations at Mt. Etna during the last two decades. From January 2011 to April 2012, 25 LF events occurred from the New South East Crater (NSEC) of Mt. Etna (Behncke et al., 2014). The LFs showed a common sequence of phases, involving mild ash-borne explosive activity, followed by Strombolian activity of variable duration (hours to days), which increased in frequency and intensity and eventually merged into a continuous jet (lava fountaining), which lasted from a few tens of minutes to hours (Behncke et al., 2014). The start of the LFs paroxysms were almost always anticipated tens of minutes to several hours by a sizeable outflow of lava from the crater (Behncke et al., 2014).

During the summer of 2011, a spring gravimeter (LaCoste & Romberg D-162) was installed about 1 km away from the summit of Mt. Etna in order to capture possible gravity changes related to the volcanic processes behind LFs (Carbone

et al., 2015). The gravimeter was installed at elevation of 3050 m and located within 2 meters from a multiparametric station of the INGV-OE permanent monitoring network. The latter (ECPN station) is equipped with a GNSS and a seismic sensor, both operating in continuous mode (`http://terremoti.ingv.it/instruments/network/IV`). The gravimeter recorded nine LFs episodes. Seven of these had good quality data, as reported in Fig. 17.

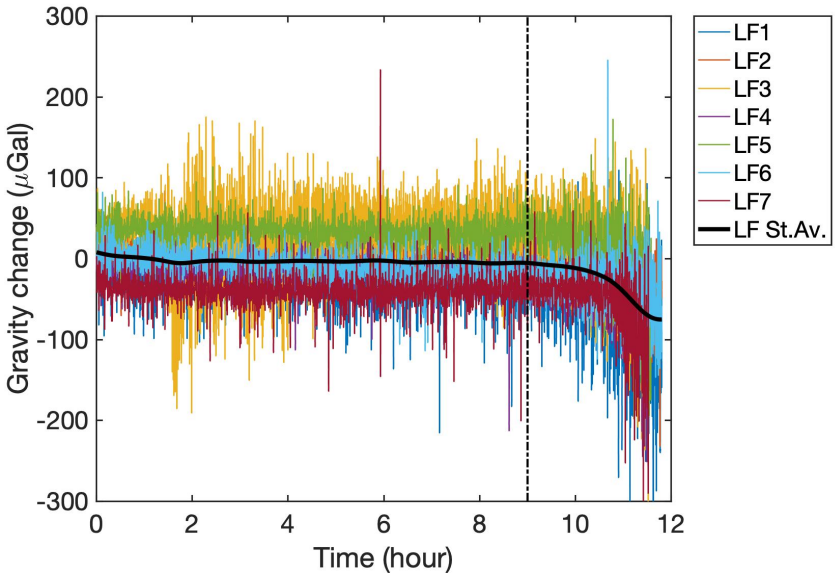

Figure 17: Gravity changes as recorded during 7 LF episodes at Mt. Etna in 2011. Thin colored lines are unfiltered data of the 7 LF episodes (LF1-7 in the legend) while thick solid line (LFSt.Av. in the legend) is the filtered, stacked and averaged time series (see text and D4.2). Dot-dashed line at 9 hour indicates the portion of gravity data used to fit the two models presented in the following sections.

All LF events are preceded a similar pattern of gravity decrease (45-65 μGal), starting 1 to 3 hours before the outbreak of the paroxysmal activity. The latter is constrained by the fast increase of seismic tremor amplitude and by thermal imaging of the NSEC (see Fig. 3 in Carbone et al., 2015). The gravity decreases observed prior to the events of LF were interpreted by Carbone et al. (2015) as due to the accumulation of gas phase within the shallowest part of the plumbing system of Mt. Etna. Specifically, gas-rich magma substituted the resident and denser magma in the magma chamber, therefore producing a localized mass decrease, detectable at the surface as a transient drop in the gravity signal. Carbone et al. (2015) modelled this process assuming a spherical source of magma placed at 1200m below the central crater and obtained a bulk volume of exsolved gas of the order of 10^9 m^3. The analysis neglected the dynamics of this gas-rich magma bubble in the volcano conduit, which is instead taken into account in the models described in the following.

In order to benchmark our models of magma ascent, we use the outcomes of deliverable D4.2 where the whole 2011 gravity time series was processed with the aim of obtaining a single averaged pre-eruptive gravity decrease (Fig. 17). In particular, the gravity time series of 7 LF events have been temporally aligned, low-pass filtered, stacked and averaged by the number of observations (see Fig.14 in D4.2). The resulting time series represents the gravity signature of the Summer 2011

LF events (Fig. 17). Moreover, each of the time series of LF events is cut to have a common length of 11.85 hours and ends when the amplitude of the volcanic tremor is too high and gravity data cannot be used any more because of the disturbance from ground shaking (see for deails Carbone et al., 2015).

In order to constrain the kinematic of magma accumulation and ascent in the conduit, we use surface observation of the eruptive parameters during LFs. From real-time radar measurement of changes in intensity and frequency of eruptive ejecta during the 2011-2015 LFs Freret-Lorgeril et al. (2018) measured an average duration of the paroxysmal activity of 180 minutes, with a minimum and maximum value of 49 and 531 minutes, respectively. The measured change of mass flow rate at the crater is thought to be representative of the magma dynamics in the conduit where a transition from slug to turbulent flow is driven by a progressively decompressed batch of gas-rich magma approaching the surface. The duration of the paroxysms can thus be used as a first order constraint of the duration of the ascent of the gas-rich magma batch in the conduit. We then consider the average estimation of 3 hours by Freret-Lorgeril et al. (2018) as representative of such magma ascending process (dot-dashed vertical line in Fig. 17). The estimated mass eruption rate (MER) of the paroxysmal activity between 2011-2015 at Mt. Etna is in the order of $10^5 - 10^6$ kg/s, and results in a total erupted mass (TEM) of $10^8 - 10^9$ kg (Freret-Lorgeril et al., 2018). We use this estimation to further constrain the dynamics of magma ascent in terms of TEM.

4.2 Model A: pressurised chamber and cylindrical conduit

The model consists of an ellipsoidal magma chamber and a vertical cylindrical conduit with base A and height H hydraulically connected via a small cylindrical valve of negligible radius R and length L (dictating the time evolution of the model), as depicted in Fig. 18.

The ellipsoidal magma chamber of volume V_c and elastic compressibility β_c is filled with magma of density ρ_m. The chamber is replenished from below by inflow of new mass δM which generates an overpressure δp_c:

$$\delta M_c = \rho_m V_c \beta_c \delta p_c \tag{5}$$

where $\beta_c = \beta_m + \beta_e$ is the total compressibility of the magma-chamber system as the sum of the magma compressibility β_m and the elastic compressibility of the chamber β_e.

At time $t = 0$ the chamber fails due to an excess pressure p_E with respect to the lithostatic pressure p_L and the cylindrical small valve allows magma to flow in the conduit modelled as an open pipe with initial pressure p_i^o. The flow of magma $Q(t) = dM_c/dt$ is driven by the evolution of magma pressure p_c in time according to the differential equation:

$$\frac{dp_c}{dt} = \frac{1}{\rho_m V_c \beta_c} \frac{dM_c}{dt} \tag{6}$$

where M_c is the mass of magma flowing out the chamber and filling the conduit.

The magma head, i.e. height of the magma in the conduit, $h(t)$, generates an inflow pressure p_i in the conduit and has a governing equation in the form:

$$\frac{dp_i}{dt} = \rho_m g \frac{dh}{dt} = -\frac{g}{A} \frac{dM_{cyl}}{dt} \tag{7}$$

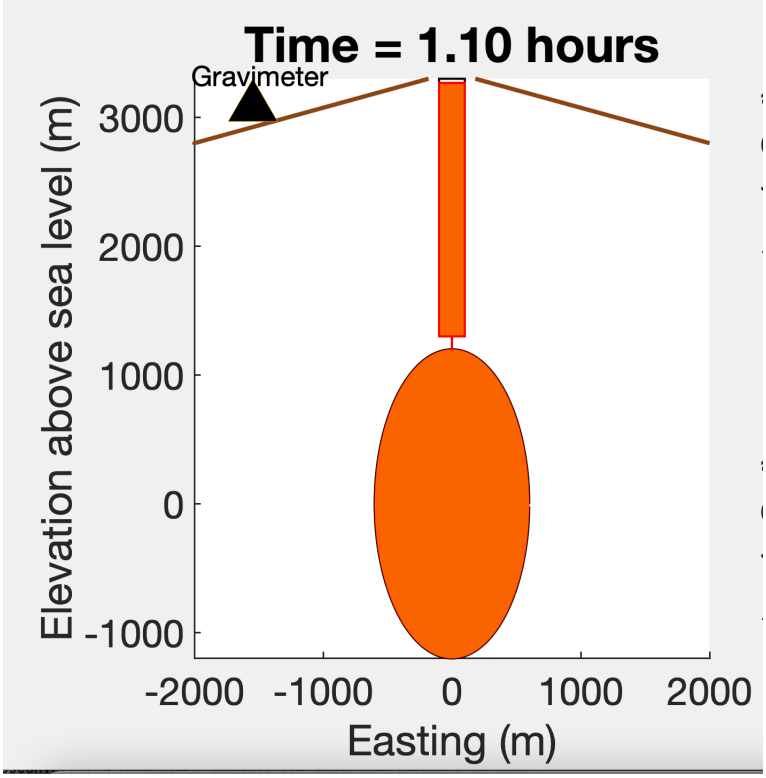

Figure 18: Model of ellipsoidal prolate magma chamber connected to a open cylinder through a small cylindrical valve of negligible volume.

assuming $dh = dV_{cyl}/A$ and $dM = \rho_m dV_{cyl}$, where g is the gravitational acceleration assumed constant. Negative sign indicates mass increase in the conduit that corresponds to a decrease of mass in the chamber such that $dM_c = -dM_{cyl}$. Therefore, since the system is closed and mass is conserved, we can combine Eq. 6 and Eq. 7 and obtain an equation that links the pressures in the chamber and in the conduit such that:

$$dp_i = -\frac{\rho_m g V_c \beta_c}{A} dp_c \tag{8}$$

which provides a general linear equation for the pressures:

$$p_i = -\frac{\rho_m g V_c \beta_c}{A} p_c + \alpha \tag{9}$$

The constant α can be determined assuming the initial open pipe condition such that $p_i^o = 0$ and the failure criterion $p_c^o = p_L + p_E$ at time $t = 0$, where $p_L = \rho_r g h^{'}$ is the lithostatic pressure and p_E is the excess pressure at which the chamber fails. Given the initial conditions, $\alpha = \frac{\rho_m g V_c \beta_c}{A}(p_L + p_E)$ and the Eq. 9 becomes:

$$p_i = -\frac{\rho_m g V_c \beta_c}{A}(p_c - p_L - p_E) \tag{10}$$

We can write the magma flow equation by assuming a Poiseuille flow in the valve for a magma with viscosity η and that $L >> R$ (see e.g. Rivalta, 2010) as:

$$\frac{dM}{dt} = -K(p_c - \Delta p_h - p_i) \tag{11}$$

where $\Delta p_h = \rho_m g L$ is the hydrostatic pressure and the constant is $K = \rho_m \pi R^4 / 8\eta L$ is derived for a incompressible Newtonian fluid in laminar flow condition. Eq. 11 depends on both p_c and p_i and cannot be solved. In order to decouple the pressure problem we can use Eq. 6 together with Eqs. 10 and 11 to obtain an equation that provides the evolution of pressure in the magma chamber such that:

$$\frac{dp_c}{dt} = -B_1(p_c - B_2) \tag{12}$$

where:

$$B_1 = \frac{\pi R^4}{8\eta L V_c \beta_c}(1 + \frac{\rho_m g V_c \beta_c}{A}) = \frac{1}{\tau} \tag{13}$$

is a characteristics time scale of the flow problem and

$$B_2 = \frac{\frac{\rho_m g V_c \beta_c (p_L - p_E)}{A} - \rho_m g L}{(1 + \frac{\rho_m g V_c \beta_c}{A})} \tag{14}$$

is a constant that depends on magma chamber geometry and location and magma compressibility and density.

The solution of Eq. 12 for time $[0, t]$ for an initial pressure in the magma chamber p_c^o has exponential form as:

$$p_c(t) = B_2 + (p_c^o - B_2)e^{-\frac{t}{\tau}} \tag{15}$$

where B_2 and τ are in Eqs. 13 and 14.

The evolution of the pressure p_i in the conduit can be obtained combining Eqs. 15 and 10 and remembering that $p_c^o = p_L + p_E$ as:

$$p_i(t) = \frac{\rho_m g V_c \beta_c}{A}(p_c^o - B_2)(1 - e^{-\frac{t}{\tau}}) \tag{16}$$

The evolution of the magma head in the conduit can be directly calculated by substituting Eq. 16 in Eq. 7 and solving for the differential equation which leads to the following exponential equation:

$$h(t) = h_o + \frac{V_c \beta_c}{A}(p_c^o - B_2)(1 - e^{-\frac{t}{\tau}}). \tag{17}$$

where h_o is the depth of the bottom of the conduit.

4.2.1 Model implementation and results

We computed the gravity changes at the surface due to mass loss via the point Compound Dislocation Model (Nikkhoo and Rivalta, 2022a) described in section 3.1. The total mass of magma in the chamber is $M_c = \rho_m V_c$ and the mass extracted from the chamber to feed the the conduit is modulated by the chamber overpressure $\Delta p_c = p_c(t) - p_c^o$, where $p_c(t)$ is the magma chamber pressure derived in Eq. 15 as:

$$\delta M_c = M_c \beta_c \Delta p_c \tag{18}$$

We calculated the potencies $dV_{x,y,z}$ of the point source model from a finite vertical prolate ellipsoid with major axis a_z and minor axes $a_x = a_y$ subject to overpressure Δp_c (Nikkhoo et al., 2017). The chamber elastic compressibility can be

calculated as $\beta_e = \frac{1}{V_c}\frac{\delta V}{\delta p}$ as the relative volume change due to a unitary change in the overpressure δp.

The gravity change due to the replenishment of the conduit is calculated via the line mass model available in Okubo (2020). The conduit is assumed to be a rigid cylinder of radius a and height H above sea level and it is assumed empty. The deformation induced by magma replenishment of the conduit is negligible (see Deliverable 4.3). The change in gravity Δg_{LM} due to the magma head ascending and recorded by a gravimeter station placed at height H_o above sea level and radial distance S from the conduit can be calculated with a line mass approximation given that $L >> a$ according to the formula:

$$\Delta g_{LM} = \pi G \rho_m a^2 \phi \left(\frac{1}{\sqrt{S^2 + (H(t) - H_o)^2)}} - \frac{1}{S} \right) + \Delta g_o \tag{19}$$

where G is the universal gravitational constant, ϕ is the magma porosity and $\Delta g_o = g(H(t) = H_o) = 0$.

We simulate the main characteristics of gas-to-magma substitution feeding the LFs in the chamber and conduit (see section 4.1) assuming a magma with relatively high compressibility, low viscosity and high porosity as reported in Table 3. We assume that failure in the chamber occurs when the excess pressure p_E is 10% of the lithostatic pressure. We simulate the gravity changes at the gravimeter station (see section 4.1) located at $H_o = 3050$m a.s.l and $S = 1545.8$m as in Fig. 18. The total gravity changes is the sum of two contributions: the mass decrease in the ellipsoidal chamber and the mass gain in the conduit. We use the model described above to simulate the time evolution of the system and relative mass transfer. Therefore, we manually tweaked the other parameters of the model to reproduce at best the stacked and averaged gravity signal in Fig. 17, the average TEM during the LF episodes and the duration of the magma ascent in the conduit of 3 hours. All the model's parameters values are reported in Table 3.

In Fig. 19 we present the model geometrical set up (left), the synthetic gravity time series for conduit and chamber (top right) and the cumulative synthetic gravity time series (bottom right). We set up the model in a 2D Cartesian system centered at the NSEC crater $[15.0041E, 37.7468N]$ and zero at the sea level (height of NSEC 3350 m). We simulate gravity at the gravity station continuously recording throughout the sequence of LFs in the summer of 2011 (ECPN multiparameteric station $[14.9865E, 37.7437N]$) with height above sea level of 3050 m. The center of the magma chamber is located at 1500 m below NSEC top to roughly reproduce the model of Carbone et al. (2015). It is a prolate ellipsoid with major vertical axis of $a_z = 500$m and $a_x = a_y = a_z/2$. The valve geometry is given in Table 3, while the conduit has 85m radius and vertical length of 1200m. We use time step of 6 minutes and stop the simulation when magma column in the conduit reaches the surface (NSEC heigth a.s.l.).

The results of the modelled time series of gravity changes are reported in Fig. 19. The gravity time series due to the mass extracted from the magma chamber follows the exponential curve of the overpressure Δp_c in Eq 18 (top right panel in Fig. 19). The overall amplitude of the gravity anomaly due to the chamber mass loss is about 80 μGal. The gravity signal simulated in the conduit predicted by the line mass model in Eq. 19 rapidly increases as the magma column rises in the conduit reaching

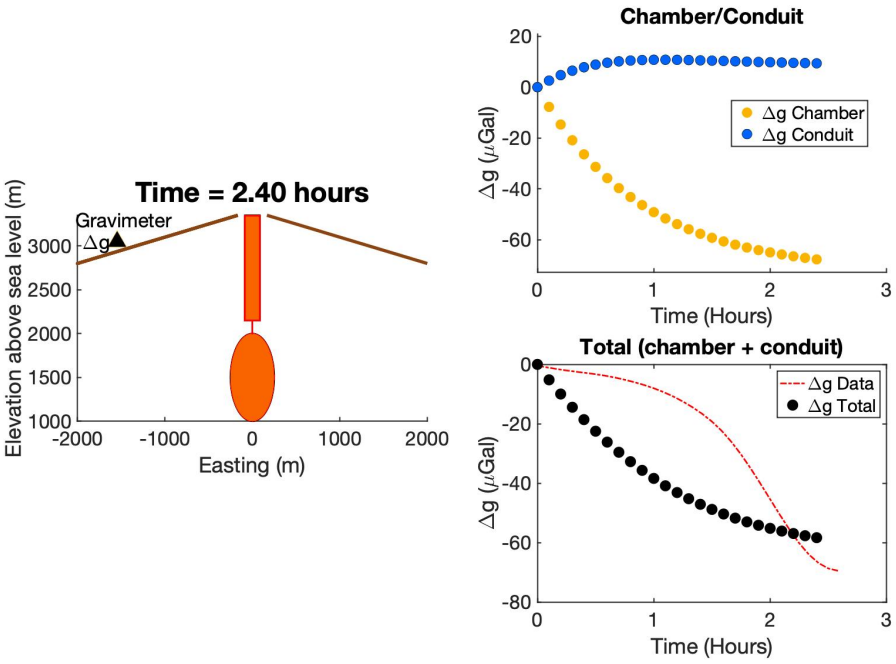

Figure 19: Model of ellipsoidal prolate magma chamber connected to a open cylinder through a small cylindrical valve of negligible volume. Left panel is geometry of the model set-up. Top right panel is the individual contribution of gravity changes of the conduit and magma chamber. The gravimeter is X=-1545.8m and at 3050 m height above sea level. Bottom left panel is the total gravity (circles) with superimposed the stacked and averaged gravity data (dot-dashed line).

its maximum at the gravimeter height; once the magma head overcomes the station, the gravity gradually decreases as the added mass attracts the gravimeter upward producing a decrease in the gravity signal (top right panel in Fig. 19). The conduit contributes to the gravity change with a peak-to-peak change in the order of 10 μGal. The total simulated gravity time series (bottom right panel in Fig. 19) is the sum of the magma chamber mass loss and conduit mass increase. This time series is dominated by the chamber signals and roughly reproduces the overall gravity decrease in the data ($\sim$80μGal), but it cannot reproduce the convex shape of the measured anomaly before each 2011 LF. Finally, the total mass extracted from the chamber (Eq. 18) is 7.8×10^{10} kg, i.e., one order of magnitude higher than the average TEM of the 2011-2015 LFs at Mt. Etna (Freret-Lorgeril et al., 2018), but same order of magnitude as estimated by Carbone et al. (2015) to explain the gravity drops of about 50μGal.

4.3 Model elastic dislocation

We model the magma ascending in the volcano edifice and feeding the LFs using a triaxial dislocation model known as Compound Dislocation Model (CDM) developed in Nikkhoo et al. (2017) coupled to the Okubo model for elastic dislocation (Okubo, 1992; Beauducel, 2012). The CDM is composed of three mutually orthogonal rectangular dislocations (RDs) that represents expansion of a triaxial source Nikkhoo et al. (2017). The three mutually orthogonal tensile RDs (Fig. 20) are

Name	Symbol	Value
Shear modulus	μ	10^9 Pa
Lame's first parameter	λ	10^9 Pa
Gravity acceleration	g	9.8 m/s^2
Free-air gradient	γ	0.3086 10^{-5} s$^{-}2$
Rock density	ρ_r	3000 kg/m^3
Magma density	ρ_m	2700 kg/m^3
Magma compressibility	β_m	10^{-8} Pa^{-1}
Magma porosity (conduit)	Φ	0.1
Viscosity	η	1 Pa s
Valve Radius	R	0.5 m
Valve Length	L	150 m
Conduit Length	H	1200 m
Conduit Length	a	85 m
Ellipsoid vertical axis	a_z	500 m
Ellipsoid horizontal axis	a_x	250 m
Ellipsoid horizontal axis	a_y	250 m

Table 3: Parameters of the chamber conduit model.

constrained to either expand or contract together and the strength of each tensile dislocation is determined by its potency, defined as the product of dislocation surface area and opening (Aki and Richards, 2002; Nikkhoo et al., 2017). The original CDM (Nikkhoo et al., 2017) has been here implemented to calculate deformation and gravity changes using the Okubo (1992) dislocation model and the routines provided by Beauducel (2012). Differently from the CDM model, it allows rotation only around the vertical axis of the Cartesian reference system by a given strike angle (ω_z in Fig. 20). The model has 11 parameters: three location coordinates, three dimensions of the rectangular dislocations (a, b and c in Fig. 20), strike angle (North to East angle), opening, the Poisson ratio ν and rock and magma density. Since in our modeling the RD will approach the free surface we are forced to use a finite dislocation model rather than the point source approximation discussed in section 3.1.

We fix the Cartesian X, Y, Z reference system in Fig. 20 to be *East*, *North* and *Up*. In order to simulate a batch of gas-rich magma propagating upward in the volcano edifice, we use only one vertical RD by collapsing the dimension of the horizontal dislocation to zero ($a \approx 0$ in Fig. 20), where the spatial orientation of RD is given by the strike angle measured North to East.

In order to calculate the opening of the single dislocation for a given volume of magma V_m, we assume that the RD can be approximated at first order by a penny-shaped crack and follow the approach of Davis et al. (2020) for a 3D crack propagating in a self-sustained manner to infer the crack geometry. Davis et al. (2020) derived the size and pressure of a vertical penny-shaped crack of radius c and volume V in an elastic medium, subject to the stress gradient $\Delta\gamma = (\rho_r - \rho_m)g$, where ρ_r and ρ_m are rock and magma density respectively and g is the acceleration of gravity, held constant. The main assumption is that the stress intensity K_I at its upper tip equals the rock fracture toughness K_c and it is zero at the lower tip. The elastic parameters of the medium control the aperture of the crack and the fracture

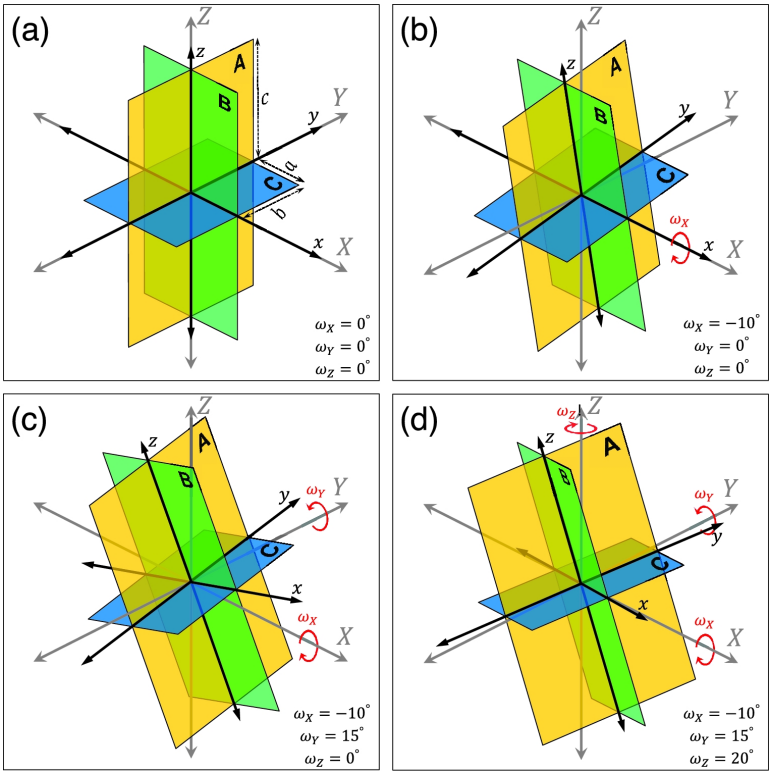

Figure 20: Compound dislocation model CDM. The structure of the CDM composed of three orthogonal RDs (the yellow, green and blue planes), labelled as 'A', 'B' and 'C'. The XYZ coordinate system is Earth-fixed and the xyz coordinate system is fixed to the CDM. The ωX, ωY and ωZ are angles of rotation about the X, Y and Z axes, respectively. Examples of a CDM with the semi-axes a, b and c along the x, y and z axes, respectively, and different rotation angles are illustrated in panels a-d. The rotation angles in each case are indicated on the bottom right of each panel. Fig. 3 reproduced from Nikkhoo et al. (2017).

radius is thus given by:

$$c = \left(\frac{3\sqrt{\pi} K_c}{8\Delta\gamma} \right)^{2/3} \tag{20}$$

We directly calculated the fracture's opening as $\Delta u = V_m/(\pi c^2)$ by using Eq. 20 and assuming $K_c = 10^8$Pa m$^{1/2}$. We finally impose the edge of the tensile RD (considered squared) to be equal to c and an opening of Δu.

We consider the magma inside the tensile RD as a two phases mixture of a melt and gas components with densities ρ_l and ρ_g, respectively. The gas phase within the ascending batch of magma undergoes expansion due to decompression, while no gas exsolution in the mixture is assumed. In order to keep the model general and dependent on very few parameters, we do not choose a specific magma composition. Rather, we assume that vesicularity depends only on pressure. We then calculate the magma density, ρ_m, of a batch of magma with mass M and volume V_m as the sum of the densities of its melt and gas phases weighted by the respective mass fractions at given depth z:

$$\frac{1}{\rho_m(z)} = \frac{V_m}{M} = \frac{V_g}{M_g}\frac{M_g}{M} + \frac{V_l}{M_l}\frac{M_l}{M} = \left(\frac{\chi RT}{M_{mol} p(z)} + \frac{1-\chi}{\rho_l} \right) \tag{21}$$

where $\rho_l = \rho_0 \exp(\beta_l p(z))$ is the melt density and the gas is ideal with $\chi = M_g/M$ gas mass fraction. R and T are ideal gas constant and temperature (in °K), while M_{mol} is the average molar mass of the gas phase. $p(z) = p_{lith}(z) - p_0$ is the depth dependent pressure ($p_{lith} = \rho_{rock} g z$), where z is depth and p_0 is reference pressure at the surface. The initial gas mass fraction χ_0 is set at the reservoir depth at a value depending on the type of magma, and ρ_l and β_l are density and compressibility of the melt phase at pressure p_0.

4.3.1 Model implementation and results

The kinematic of the ascending batch of gas-rich magma is largely unknown since no geophysical observable can directly inform on this processes. However, as previously discussed, we can use the average duration of 3 hours for the 2011-2015 paroxysms at Mt. Etna as a proxy on the duration of the ascending gas-rich magma batch (see section 4.1). This is compatible with the 1-3 hours anomaly decrease of gravity measured at Mt. Etna in the Summer 2011 LF episodes (see Fig. 17). Therefore, we assume that a duration T_g of 3 hours as representative of the gas-rich magma uplift process and, given a starting depth for the RD, we can calculate the average ascending velocity. As by convention of the CDM model, we use the depth Z_0^{in} of its center as initial depth, the RD velocity is $v_{RD} = Z_0^{in}/T_g$.

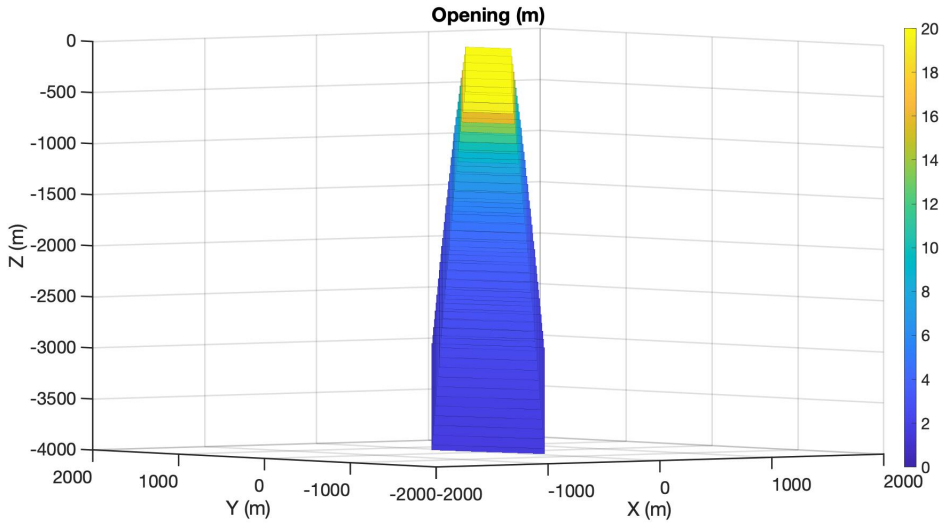

Figure 21: Example of ascending tensile RD. Color-code is the opening in meters and Cartesian axis are X=East, Y=North and Z=Up.

As represented in Fig 21, the RD starts from a initial depth Z_0^{in} and propagates upward with a constant velocity v_{RD}. In order to constrain the mass of magma in the ascending RD, we assume an average $MER \sim 10^6$ kg s^{-1} measured during the LFs in 2011-2015 (Freret-Lorgeril et al., 2018), which, for a duration $T_g = 3$ hours, retrieved from the gravity signal, produces a total erupted mass $TEM = MER \times T_g = 1.08 \times 10^{10}$ kg. This estimate is on order of magnitude larger than the average TEM estimated by Freret-Lorgeril et al. (2018) for the 2011-2015 LFs, but only slightly larger of the maximum value of TEM of about 7×10^9. It is also on the same order of magnitude as the value estimated by Carbone et al. (2015) to produce the gravity drop of about $50 \mu Gal$. We finally calculate the volume

of magma $V_m = TEM/\rho_m(z)$ at depth Z_0^j of the ascending RD, where j are the incremental discrete steps until the upper edge of the RD reaches the surface. We want to remark that the depth-dependent decrease of magma density ρ_m - due to decompression-induced gas-expansion - incrementally reduces the crack radius (see Eq. 20) and consequently increases the RD opening $\Delta u = V_m/(\pi c^2)$ in order to conserve the volume of the gas-rich magma batch.

In order to use the model for simulating the time series from the gravity station, we set up the model in the following way. We fix the elastic and initial magma properties as reported in Table 4 and we use as free parameters the starting depth and strike angle of the RD. We do not set up a formal optimization scheme for this model since the availability of only a single time series of gravity data (thick line in Fig. 17). We rather simulate stochastically the initial depth and strike angle in order to scan the model's parameters space and find the single pair of parameters that reproduce the average gravity anomaly at best. We therefore run 10000 simulation of the model with initial depth drawn from a uniform distribution between $[1000, 3000]$ meters below Mt. Etna edifice from its top, and strike angle uniformly distributed between $[0°, 360°]$. The chosen depth range derives from depths previously inferred for the magma feeding system of the LFs of 2011 (Carbone et al., 2015; Bonaccorso et al., 2013). We instead allow the strike angle to explore all the possible angles. We used a Earth fixed Cartesian reference system centered at the NSEC $[15.0041E, 37.7468N]$ and the gravity signal is simulated at the gravity station $[14.9865E, 37.7437N]$ with height above sea level of 3050 m, that is the free surface of the RD model. We assume that the gravity change is only due to the ascending gas-rich magma of density $\rho_m(z)$ in Eq. 21.

Name	Symbol	Value
Shear modulus	μ	10^9 Pa
Lame's first parameter	λ	10^9 Pa
Gravity acceleration	g	9.8 m/s^2
Free-air gradient	γ	0.3086 10^{-5} s$^-$2
Rock density	ρ_r	2700 kg/m^3
Magma density (initial)	ρ_m	2500 kg/m^3
Liquid density (initial)	ρ_l	2700 kg/m^3
Liquid compressibility	β_l	2 x 10$^-$10 Pa$^-$1
Initial gas fraction	χ_0	0.015 wt%
Temperature	T	1473° K
Molar mass	M_{mol}	0.022
Fracture toughness	K_c	10^8 Pa m$^{1/2}$

Table 4: Parameters of the elastic dislocation model.

The results of the simulated time series are reported in Fig. 22 together with the decompression induced density decrease and the uplift predicted at the gravity station. The variable temporal lengths of each time series in Fig. 22 is because we stop each simulation when the upper edge of the RD reaches the gravimeter height, i.e. free surface of the CDM model. The model predicts gravity change time series with increasing or decreasing gravity at the stations of variable length and pattern depending on the initial depth and strike parameters. The calculated density profiles from Eq. 21, in input to the RD models, ranges between about

2000 kg/m^3, at the initial depths, and 500 kg/m^3 at the station height, about 300 m below NSEC. Those values are consistent with density estimates of lithic ejecta during LF episodes (Freret-Lorgeril et al., 2018). The simulated elevation changes at the gravimeter are in the order of a few to tens of centimeters either predicting uplift or minor subsidence depending on the strike orientation of the RD.

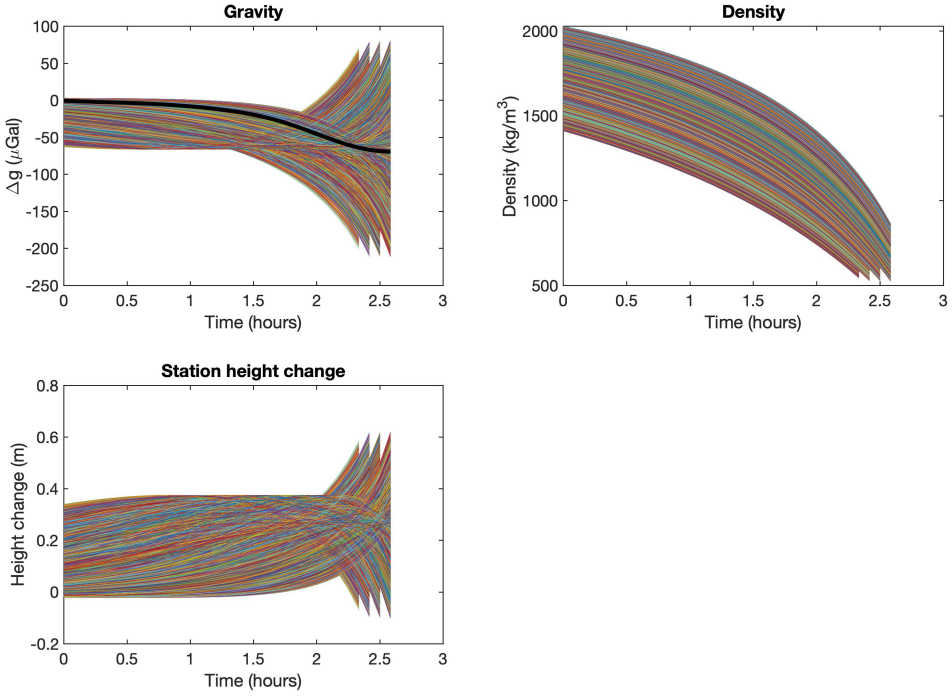

Figure 22: Monte Carlo realization of the RD model for time series of total gravity change (top left), density profile (top right) and uplift at gravity station (bottom left). Thin colored line in each panel are 10000 Monte Carlo simulation of the model. In the top-left panel the thicker black line are the averaged gravity data presented in Fig. 17. All time series are simulated every time step of 5 minutes and the average gravity data are decimated with the same time step.

We minimize the root mean square error (RMS) of the simulated and averaged gravity time series in order to infer the best-fit pair of depth and strike that are able to reproduce the time series of the averaged gravity data in Fig. 17 at best. The RMS value are reported in Fig.23, for each pair of depths and strikes in the Monte Carlo simulation. The RMS values show minima at depths $[2400, 3000]$m and strikes $220° \pm 10°$ and $300° \pm 10°$ (the latter with a periodicity of $180°$).

The global minimum of RMS corresponds to a starting depth of 2875 m and strike of 297°. As shown in Fig.24, the fit of the predicted time series of gravity changes to the observed data is almost perfect with a RMS of 15.12. The inferred depth value is compatible with the position of the ellipsoidal magma chamber inverted using tilt data during the LFs of 2011 (Bonaccorso et al., 2013), but 1500 m deeper than the source used by Carbone et al. (2015) to explain the pre-fountain gravity decreases. The best strike direction of 297° is compatible with the NNW-SSE orientation of the eruptive vents of NSEC during the LF episodes in 2011 (Behncke et al., 2014).

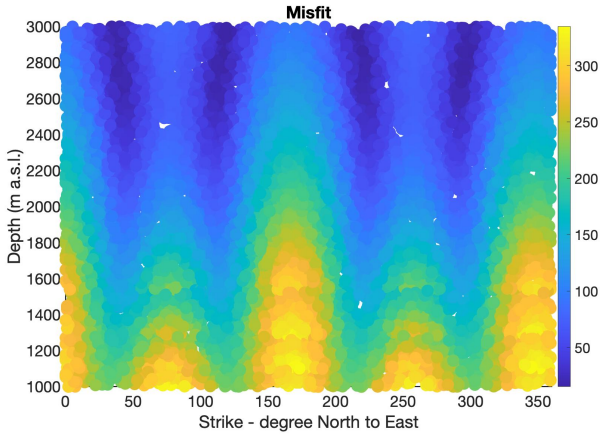

Figure 23: Monte Carlo realization of strike and depth parameters of the model with color-coded misfit values calculated as RMS. Please note that minima (dark-blue at depth of 2800-3000 m) have a π periodicity as expected.

A close inspection to the simulated time series of gravity change once it is decomposed in its fundamental contribution - free-air, dilatation/contraction of the host rocks, surface mass redistribution, cavity formation and mass change, see section 3.1 - indicates that the major contribution to the gravity decrease comes from the free-air effect (Fig. 25). This results is largely expected since the RD best model predict a maximum of about 25cm uplift at the gravimeter station (Fig. 24). The RD vertical displacement lift the gravimeter upwards producing a decrease of the measured gravity signal that dominates on the total gravity signal with respect to all the other components. The large part of the uplift is short and lasts about one hour considering a detection threshold of 5 cm (few μGal) at the gravity station. The large and transients deformation is expected since we use RD model in an elastic half space approaching the free surface. However, the rock properties in the upper layer of the Mt. Etna edifice are unlikely to be pure elastic and thus the predicted uplift is likely an overestimation of the true one. Carbone et al. (2015) reported that no or little deformation (few cm) was observed at the GNSS station co-located with the gravity station during the LFs in Summer 2011. However, our simulation involves a transient and localized deformation, occurring over a short time scale and confined around the active crater, which may remain undetected, unless a dense network of high-rate GNSS sensors is employed. Useful information for validating the proposed RD model could come from strain data and a study is ongoing to explore this possibility.

4.4 Learning points

1. The magma chamber-conduit model is able to reproduce the peak-to-peak anomaly but not the shape of gravity decrease during LFs and requires high magma compressibility.

2. The major contribution to the gravity signal in the magma-chamber conduit setting derives from the chamber but only if the magma in the conduit has a high gas content.

3. The mass extracted from the chamber via the pressure model strongly depends

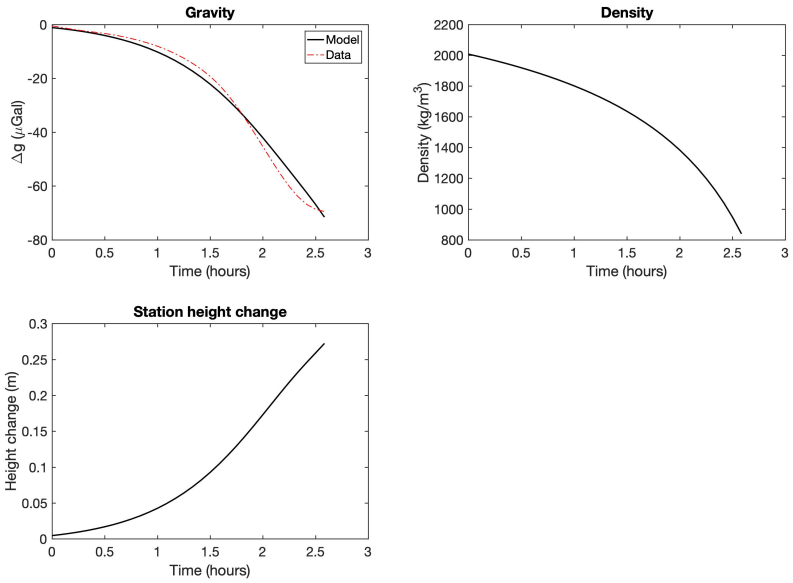

Figure 24: As in Fig. 22 but for the best-fit realization of the Monte Carlo simulation for depth=2875 m and strike=297°. Time series of total gravity change (top left), density profile (top right) and uplift at gravity station (bottom left). Thin black line in each panel are best-fit simulation of the model. In the top-left panel the dot-dashed line is the averaged gravity data presented in Fig. 17.

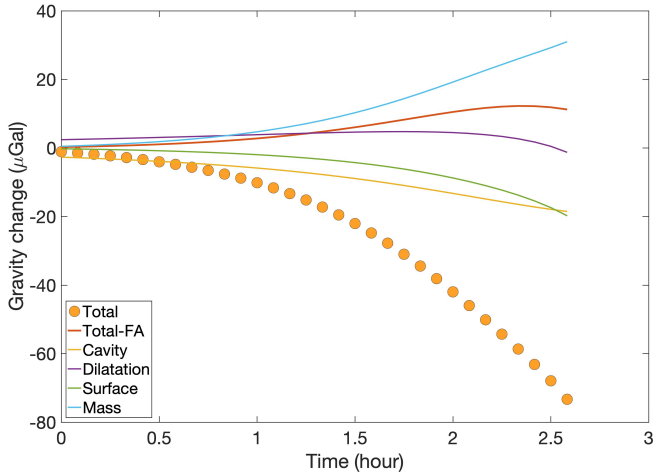

Figure 25: Total gravity change signal at as in the top left panel Fig. 24 (orange circles). The solid line is the total gravity minus the Free-Air gravity in order to highlight the major contribution of station uplift in the total gravity signal.

on the volume of the ellipsoid (i.e. dimension of the ellipsoid), location and magma properties.

4. The magma chamber-conduit model is not fully suitable to describe the gravity decreases observed prior to each LF in 2011; however, it may provide useful indications to interpret volcano-related gravity changes observed with extended arrays of observation points.

5. The elastic RD model, that simulate an ascending batch of gas-rich magma in the volcano, can almost perfectly reproduce the observed gravity data, for a realistic set of model parameters; however, the major contribution to the gravity decrease is given by the strong transient deformation affecting the area where the gravimeter is installed.

6. Such a strong and short-lasting transient deformation is non supported by the available deformation data; however, we plan to review the deformation data acquired at Mt. Etna during the summer of 2011, with the aim of checking for possible fast changes which may have remained undetected.

7. We are also currently working on the comparison between the deformation predicted by our RD model and the strain data available for the LF episodes at Mt. Etna in 2011 and later.

8. In general, without a dense network of gravity and deformation stations close to the eruptive center it is difficult to validate the forward simulation of the two models.

9. Both models are computationally inexpensive and adapt to generate synthetic scenario-based gravity time series for real and near-real time applications, a key ingredient for incorporating gravity data into volcano hazard analysis.

5 Conclusive remarks

In this document we explore the potential of continuous gravity observations as a tool for short- to mid-term volcano hazard analysis. We focus on LFs, which pose several threats in terms of hazard and have been among the most recurrent features of the volcanic activity of Mt. Etna during the last two decades. We applied two different approaches to fulfill the scopes of the deliverable.

In the framework of the "data-driven" approach (section 2), we perform a study mainly focused on (i) the gravity data collected at Mt. Etna between February and October 2021, a period when more than 60 LFs were produced by one of the summit craters of the volcano and (ii) the eruptive source parameters retrieved by remote sensing techniques for some of the 2021 LFs.

A recurrent feature in the signal from the two iGrav SGs, installed at distances of 3.5 and 6.5 km from the summit vents of Mt. Etna, is a small gravity decrease, taking place during the last 6-24 hours before each LF. We cross-analyze the characteristics of these pre-fountaining gravity changes with the data from remote sensing observations. We highlight a weak, but significant, correlation between amplitude of the observed gravity decreases and the mass of tephra plus lava emitted during each LF episode. The correlation suggests that a physical link may exist between the amount of volatiles involved in the underground gas-to-magma substitution, before the breakout of each LF, and the final amount of erupted material. This link should be further investigated, possibly through data from an array of gravimeters at closer distance from the active crater.

The AQG-B installed at Mt. Etna under NEWTON-g (Antoni-Micollier et al., 2022) provides data with lower precision than data from the SGs and this prevents

the detection of the small gravity changes described above. Nevertheless, the AQG-B features an active vibration compensation system and it is less affected than SGs by strong ground shaking during LFs. Indeed, on some occasions, gravity changes can be recognized in the signal from the AQG-B during the last 4-5 hours before the climatic phase of the LFs. Such changes cannot be observed in the SGs recordings, since the amplitude of the volcanic tremor at the installation site is above a threshold which hamper the use of gravity data. The complementary of the signals from gravimeters with different characteristics is another issue deserving further consideration, especially for the implications on the study of volcanic processes accompanied by high levels of volcanic tremor.

Using the continuous gravity data from the three instruments recording at Mt. Etna in 2021, we also highlight a common gravity change, occurring during a 2-month interval when a the edifice deflation was in a deflation phase. The joint analysis of gravity and deformation data provides insight that could not be assessed if only one parameter was considered.

In the framework of the "model-based" approach, we (i) lay down a theoretical framework for the joint inversion of gravity and deformation data, involving new analytic formulations developed under NEWTON-g (section 3) and (ii) develop scenario-based models able to generate synthetic time series of gravity changes that could take place before the breakout of LFs (section 4).

The theoretical framework discussed in section 4 involves new analytical formulations that can be used to calculate, consistently and comprehensively, all contributions to deformation and gravity changes induced by underground pressure/mass sources. The use of these formulations does not require a-priori assumptions on the shape of the source body, implying that a wide range of source shapes can be checked in the frame of a single inversion run. Bias on the inferred source parameters, due to misleading assumptions on the shape of the source, are thus largely eliminated. It is noteworthy that the lack of analytical solution for gravity changes associated to triaxial deformation was a recognized gap in volcano geodesy, which has now been filled. We also present a new joint inversion approach, involving an alternative way of applying the free-air correction to the gravity data.

Two scenario-based models are discussed in section 5, one involving the flux of magma from a pressurized magma chamber to the cylindrical conduit on top of it. The other assumes a rise of the magma from depth to the surface, through a vertical tensile crack model. The synthetic time series produced through the application of these models are compared with the averaged gravity anomaly observed before each LF in the summer 2011 sequence. This comparison highlights pros and cons of the two scenario-based models, thus opening the way towards a better understanding of the processes behind the observed pre-LF gravity changes. Indeed, while an approach based exclusively on the detection of redundant anomalies in the gravity time series, which are likely to precede paroxysmal phases of the volcanic activity, produces valuable results for volcano hazard assessment. However, a full understanding of the cause-effect relationship between underground volcanic processes and gravity changes observed at the surface requires the application of model-based approaches aimed at quantitatively address the above relationship. We thus plan to perform further work aimed at improving the scenario-based models presented here and develop new ones, to further enhance the possibilities of a continuous volcano gravimetry, eventually leading to a more comprehensive inclusion of gravity data

into probabilistic volcano hazard assessment and early warning.

References

Aki, K. and Richards, P. G. (2002). *Quantitative seismology*. University Science Books, Sausalito, California, 2nd edition.

Alparone, S., Andronico, D., Lodato, L., and Sgroi, T. (2003). Relationship between tremor and volcanic activity during the southeast crater eruption on mount etna in early 2000. *Journal of Geophysical Research: Solid Earth*, 108(B5).

Andronico, D., Behncke, B., De Beni, E., Cristaldi, A., Scollo, S., Lopez, M., and Lo Castro, M. D. (2018). Magma budget from lava and tephra volumes erupted during the 25-26 october 2013 lava fountain at mt etna. *Frontiers in Earth Science*, 6:116.

Andronico, D., Scollo, S., Cristaldi, A., and Lo Castro, M. D. (2014). Representivity of incompletely sampled fall deposits in estimating eruption source parameters: a test using the 12–13 january 2011 lava fountain deposit from mt. etna volcano, italy. *Bulletin of volcanology*, 76(10):1–14.

Antoni-Micollier, L., Carbone, D., Ménoret, V., Lautier-Gaud, J., King, T., Greco, F., Messina, A., Contrafatto, D., and Desruelle, B. (2022). Detecting volcano-related underground mass changes with a quantum gravimeter. *Earth and Space Science Open Archive*.

Beauducel, F. (2012). Okubo: Gravity change due to shear and tensile faults. http://www.ipgp.fr/ beaudu/matlab.html. MATLAB code.

Behncke, B., Branca, S., Corsaro, R. A., De Beni, E., Miraglia, L., and Proietti, C. (2014). The 2011–2012 summit activity of mount etna: Birth, growth and products of the new se crater. *Journal of Volcanology and Geothermal Research*, 270:10–21.

Bonaccorso, A. and Calvari, S. (2017). A new approach to investigate an eruptive paroxysmal sequence using camera and strainmeter networks: Lessons from the 3–5 december 2015 activity at etna volcano. *Earth and Planetary Science Letters*, 475:231–241.

Bonaccorso, A., Calvari, S., Linde, A., and Sacks, S. (2014). Eruptive processes leading to the most explosive lava fountain at etna volcano: The 23 november 2013 episode. *Geophysical Research Letters*, 41(14):4912–4919.

Bonaccorso, A., Currenti, G., Linde, A., and Sacks, S. (2013). New data from borehole strainmeters to infer lava fountain sources (etna 2011–2012). *Geophysical Research Letters*, 40(14):3579–3584.

Bonadonna, C., Folch, A., Loughlin, S., and Puempel, H. (2012). Future developments in modelling and monitoring of volcanic ash clouds: outcomes from the first iavcei-wmo workshop on ash dispersal forecast and civil aviation. *Bulletin of volcanology*, 74(1):1–10.

Calvari, S., Biale, E., Bonaccorso, A., Cannata, A., Carleo, L., Currenti, G., Di Grazia, G., Ganci, G., Iozzia, A., Pecora, E., et al. (2022). Explosive paroxysmal events at etna volcano of different magnitude and intensity explored through a multidisciplinary monitoring system. *Remote Sensing*, 14(16):4006.

Calvari, S., Cannavò, F., Bonaccorso, A., Spampinato, L., and Pellegrino, A. G. (2018). Paroxysmal explosions, lava fountains and ash plumes at etna volcano: Eruptive processes and hazard implications. *Frontiers in Earth Science*, 6:107.

Cannavo', F., Sciotto, M., Cannata, A., and Di Grazia, G. (2019). An integrated geophysical approach to track magma intrusion: The 2018 christmas eve eruption at mount etna. *Geophysical Research Letters*, 46(14):8009–8017.

Carbone, D., Antoni-Micollier, L., Hammond, G., de Zeeuw-van Dalfsen, E., Rivalta, E., Bonadonna, C., Messina, A., Lautier-Gaud, J., Toland, K., Koymans, M., et al. (2020). The newton-g gravity imager: Toward new paradigms for terrain gravimetry. *Frontiers in Earth Science*, 8:573396.

Carbone, D., Cannavó, F., Greco, F., Reineman, R., and Warburton, R. J. (2019). The benefits of using a network of superconducting gravimeters to monitor and study active volcanoes. *Journal of Geophysical Research: Solid Earth*, 124(4):4035–4050.

Carbone, D., Poland, M. P., Diament, M., and Greco, F. (2017). The added value of time-variable microgravimetry to the understanding of how volcanoes work. *Earth-Science Reviews*, 169:146–179.

Carbone, D., Zuccarello, L., Messina, A., Scollo, S., and Rymer, H. (2015). Balancing bulk gas accumulation and gas output before and during lava fountaining episodes at mt. etna. *Scientific reports*, 5(1):1–11.

Corradini, S., Montopoli, M., Guerrieri, L., Ricci, M., Scollo, S., Merucci, L., Marzano, F. S., Pugnaghi, S., Prestifilippo, M., Ventress, L. J., et al. (2016). A multi-sensor approach for volcanic ash cloud retrieval and eruption characterization: The 23 november 2013 etna lava fountain. *Remote Sensing*, 8(1):58.

Currenti, G. (2014). Numerical evidence enabling reconciliation gravity and height changes in volcanic areas. *Geophysical Journal International*, 197(1):164–173.

Currenti, G. (2018). Viscoelastic modeling of deformation and gravity changes induced by pressurized magmatic sources. *Journal of Volcanology and Geothermal Research*, 356:264–277.

Currenti, G., Del Negro, C., and Ganci, G. (2007). Modelling of ground deformation and gravity fields using finite element method: an application to Etna volcano. *Geophysical Journal International*, 169(2):775–786.

Davis, T., Rivalta, E., and Dahm, T. (2020). Critical fluid injection volumes for uncontrolled fracture ascent. *Geophysical Research Letters*, 47(14):e2020GL087774.

De Beni, E., Behncke, B., Branca, S., Nicolosi, I., Carluccio, R., Caracciolo, F., and Chiappini, M. (2015). The continuing story of etna's new southeast crater (2012–2014): Evolution and volume calculations based on field surveys and aerophotogrammetry. *Journal of Volcanology and Geothermal Research*, 303:175–186.

Freret-Lorgeril, V., Bonadonna, C., Corradini, S., Donnadieu, F., Guerrieri, L., Lacanna, G., Marzano, F. S., Mereu, L., Merucci, L., Ripepe, M., et al. (2021). Examples of multi-sensor determination of eruptive source parameters of explosive events at mount etna. *Remote Sensing*, 13(11):2097.

Freret-Lorgeril, V., Donnadieu, F., Scollo, S., Provost, A., Fréville, P., Guéhenneux, Y., Hervier, C., Prestifilippo, M., and Coltelli, M. (2018). Mass eruption rates of tephra plumes during the 2011–2015 lava fountain paroxysms at mt. etna from doppler radar retrievals. *Frontiers in Earth Science*, 6:73.

Guerrieri, L., Merucci, L., Corradini, S., and Pugnaghi, S. (2015). Evolution of the 2011 mt. etna ash and so2 lava fountain episodes using seviri data and vpr retrieval approach. *Journal of volcanology and geothermal research*, 291:63–71.

Marzano, F., Mereu, L., Scollo, S., Donnadieu, F., and Bonadonna, C. (2020). Tephra mass eruption rate from x-band and l-band microwave radars during the 2013 etna explosive lava fountain. *IEEE Trans. Geosci. Remote Sens*, 58:3314–3327.

Marzano, F. S., Picciotti, E., Vulpiani, G., and Montopoli, M. (2011). Synthetic signatures of volcanic ash cloud particles from x-band dual-polarization radar. *IEEE transactions on geoscience and remote sensing*, 50(1):193–211.

Ménoret, V., Vermeulen, P., Le Moigne, N., Bonvalot, S., Bouyer, P., Landragin, A., and Desruelle, B. (2018). Gravity measurements below 10- 9 g with a transportable absolute quantum gravimeter. *Scientific reports*, 8(1):1–11.

Mereu, L., Scollo, S., Bonadonna, C., Freret-Lorgeril, V., and Marzano, F. S. (2020). Multisensor characterization of the incandescent jet region of lava fountain-fed tephra plumes. *Remote Sensing*, 12(21):3629.

Montopoli, M. (2016). Velocity profiles inside volcanic clouds from three-dimensional scanning microwave dual-polarization doppler radars. *Journal of Geophysical Research: Atmospheres*, 121(13):7881–7900.

Nikkhoo, M. and Rivalta, E. (2022a). Analytical solutions for gravity changes caused by triaxial volumetric sources. *Geophysical Research Letters*, 49(8):e2021GL095442. e2021GL095442 2021GL095442.

Nikkhoo, M. and Rivalta, E. (2022b). Surface deformations and gravity changes caused by pressurized finite ellipsoidal cavities. *Geophysical Journal International*. ggac351.

Nikkhoo, M., Walter, T. R., Lundgren, P. R., and Prats-Iraola, P. (2017). Compound dislocation models (cdms) for volcano deformation analyses. *Geophysical Journal International*, page ggw427.

Okubo, S. (1992). Gravity and potential changes due to shear and tensile faults in a half-space. *Journal of Geophysical Research: Solid Earth*, 97(B5):7137–7144.

Okubo, S. (2020). Advances in gravity analyses for studying volcanoes and earthquakes. *Proceedings of the Japan Academy, Series B*, 96(2):50–69.

Prata, A. and Grant, I. (2001). Retrieval of microphysical and morphological properties of volcanic ash plumes from satellite data: Application to mt ruapehu, new zealand. *Quarterly Journal of the Royal Meteorological Society*, 127(576):2153–2179.

Pugnaghi, S., Guerrieri, L., Corradini, S., and Merucci, L. (2016). Real time retrieval of volcanic cloud particles and so 2 by satellite using an improved simplified approach. *Atmospheric Measurement Techniques*, 9(7):3053–3062.

Pugnaghi, S., Guerrieri, L., Corradini, S., Merucci, L., and Arvani, B. (2012). A new simplified procedure for the simultaneous so2 and ash retrieval in a tropospheric volcanic cloud. *Atmos. Meas. Tech. Discuss*, 5:8859–8894.

Pulvirenti, F., Silverii, F., and Battaglia, M. (2021). A new analysis of caldera unrest through the integration of geophysical data and fem modeling: The long valley caldera case study. *Remote Sensing*, 13(20):4054.

Ripepe, M., Marchetti, E., Delle Donne, D., Genco, R., Innocenti, L., Lacanna, G., and Valade, S. (2018). Infrasonic early warning system for explosive eruptions. *Journal of Geophysical Research: Solid Earth*, 123(11):9570–9585.

Rivalta, E. (2010). Evidence that coupling to magma chambers controls the volume history and velocity of laterally propagating intrusions. *Journal of Geophysical Research: Solid Earth*, 115(B7).

Rose, W. I. and Durant, A. J. (2009). Fine ash content of explosive eruptions. *Journal of Volcanology and Geothermal Research*, 186(1-2):32–39.

Scollo, S., Prestifilippo, M., Bonadonna, C., Cioni, R., Corradini, S., Degruyter, W., Rossi, E., Silvestri, M., Biale, E., Carparelli, G., et al. (2019). Near-real-time tephra fallout assessment at mt. etna, italy. *Remote Sensing*, 11(24):2987.

Scollo, S., Prestifilippo, M., Pecora, E., Corradini, S., Merucci, L., Spata, G., and Coltelli, M. (2014). Eruption column height estimation of the 2011-2013 etna lava fountains. *Annals of Geophysics*, 57(2):S0214–S0214.

Segall, P. (2010). *Earthquake and volcano deformation*. Princeton University Press.

Trasatti, E. and Bonafede, M. (2008). Gravity changes due to overpressure sources in 3d heterogeneous media: application to campi flegrei caldera, italy. *Annals of Geophysics*.

Vulpiani, G., Ripepe, M., and Valade, S. (2016). Mass discharge rate retrieval combining weather radar and thermal camera observations. *Journal of Geophysical Research: Solid Earth*, 121(8):5679–5695.